iScience

CellPress

Article

Quasi-Metal for Highly Sensitive and Stable Surface-Enhanced Raman Scattering

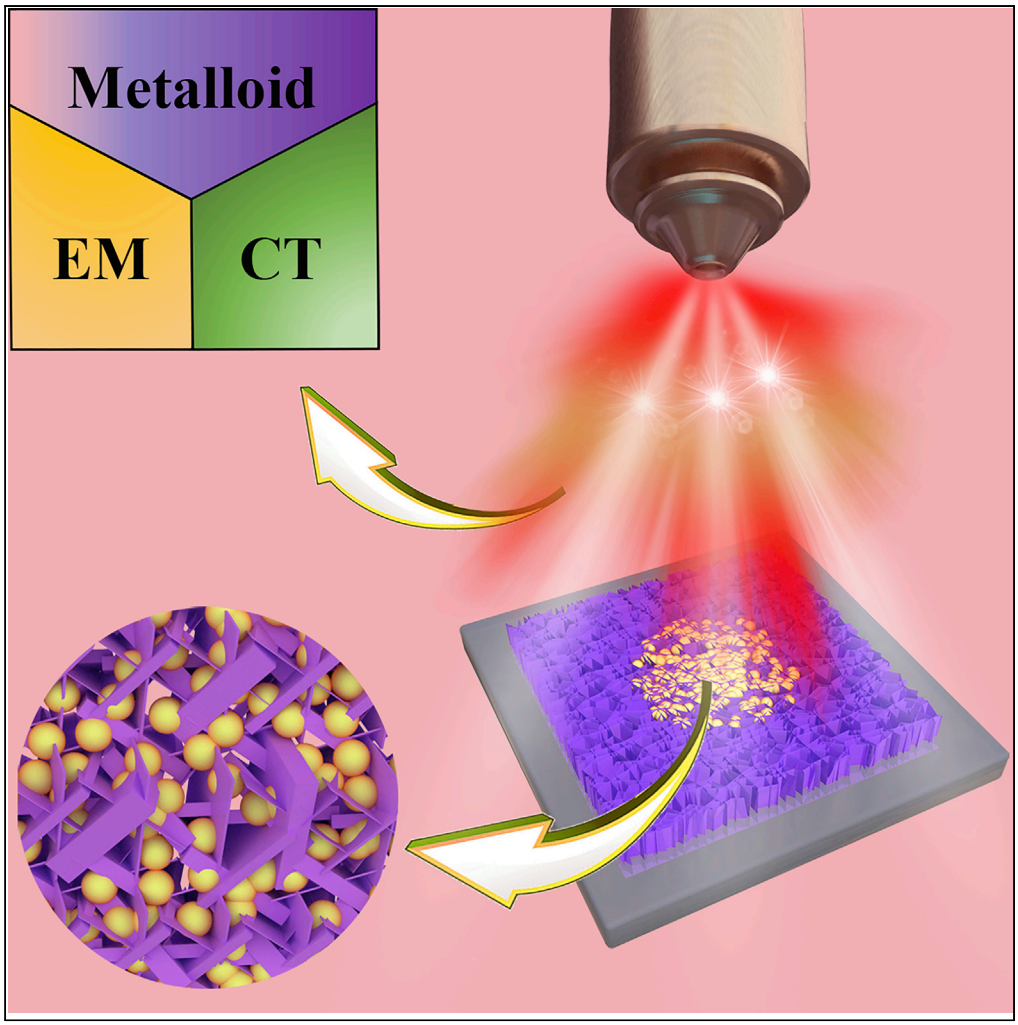

Zheng Tian, Hua Bai, Chao Chen, ..., Wenhao Fan, Wencai Yi, Guangcheng Xi

xiguangcheng@caiq.org.cn

HIGHLIGHTS

Surface-enhanced Raman scattering (SERS) on quasi-metallic VO_2

High SERS enhancement factor and low limit of detection have been achieved

Synergistic effect of electromagnetic enhancement and chemical enhancement

Tian et al., iScience 19, 836–849
September 27, 2019
https://doi.org/10.1016/j.isci.2019.08.040

iScience

CellPress

Article

Quasi-Metal for Highly Sensitive and Stable Surface-Enhanced Raman Scattering

Zheng Tian,[1,3,6] Hua Bai,[1,6] Chao Chen,[2] Yuting Ye,[1] Qinghong Kong,[3] Yahui Li,[1] Wenhao Fan,[4] Wencai Yi,[5] and Guangcheng Xi[1,7,*]

SUMMARY

Compared with the noble-metal surface-enhanced Raman scattering (SERS) substrates activated by the surface plasmon resonance (SPR)-induced electromagnetic mechanism (EM), the relative low sensitivity and stability of the chemical mechanism (CM)-based substrates are the biggest obstacles to their applications. Herein, we report that quasi-metallic VO_2 nanosheet arrays can be used as a sensitive and stable SERS substrate. The lowest detectable limit of analyte adsorbed on the VO_2 nanosheets achieves 10^{-10} M and the maximum Raman enhancement factor (EF) reaches 6.7×10^7, which is comparable with that of the noble metals. The experimental and theoretical results demonstrate that the SERS performance of the VO_2 nanosheets comes from the strong interfacial interactions based on charge transfer and the vigorous SPR effects. Our research results demonstrate that quasi-metals are very promising SERS detection platforms and reveal that CM, like EM, contributes significantly to the SERS activity of quasi-metals.

INTRODUCTION

Since Fleischmann and Van Duyne et al. groundbreakingly discovered that weak Raman signals of molecules can be drastically amplified by surface-enhanced Raman scattering (SERS) on rough silver surface (Fleischmann et al., 1974; Jeanmaire and Van Duyne, 1977; Moskovits, 1978), this technology already has become a very important label-free detection method in trace and even single-molecule levels (Nie, and Emory, 1997; Kneipp et al., 1997). As a highly sensitive, non-contact, and non-destructive technology, SERS has been widely adopted in environmental detection (Li et al., 2010; Mulvihill et al., 2008), biological imaging (Palonpon et al., 2013; Kneipp et al., 2008; Qian et al., 2008), medical diagnostics (Schlucker, 2014; Wang et al., 2012), fingerprint molecular distinguishing (Lin et al., 2009; Alvarez-Puebla and Liz-Marzan, 2012), catalytic reaction monitoring, and other fields (Peksa et al., 2015; Li et al., 2015). The traditional SERS substrate materials are based on noble-metal nanostructures with roughened surfaces (Taylor et al., 2013; Zhang et al., 2013; Kanipe et al., 2016; Phan-Quang et al., 2015), which can greatly enhance the Raman signal intensity of analyte adsorbed on the substrate surfaces with a factor of 10^6 or higher. Local field enhancement-induced surface plasmon resonance (SPR), especially the emergence of a large number of "hot spots" (high-intensity electromagnetic field regions formed at nanoscale gaps) (Zhu et al., 2016), is considered as a well-known enhancement mechanism of Raman scattering, that is, electromagnetic mechanism (EM). However, EM-based noble-metal SERS substrates are generally subjected to the considerable complex and precise preparation processes, which makes them lack the structural controllability and signal repeatability of the substrates. In addition, they also suffer from the high cost, poor biocompatibility, neglectable photocorrosion, and so on. Another universally accepted enhancement mode, chemical mechanism (CM), mainly refers to the process of charge transfer between SERS substrates and molecules adsorbed on their surfaces (Zhang et al., 2015; Quagliano, 2004; Li et al., 2013). Charge transfer will cause molecule resonance, which will greatly increase the polarizability of adsorbed molecules, and the corresponding Raman scattering cross-section will increase, resulting in the enhancement of SERS signal (Qiu et al., 2015; Cong et al., 2015; Zheng et al., 2017). Although researchers have accepted the concept that SERS is a result of EM and CM combining, it is generally believed that CM plays only a minor role since charge transfer is a short-range action.

After the first generation of SERS technology based on the noble-metal materials dominated by EM, the non-noble-metal substrates based on CM have been developed vigorously in the last 10 years, such as semiconductor nanostructures including Cu_2O (Lin et al., 2017, 2018), Si (Wang et al., 2011), $W_{18}O_{49}$ (Cong et al., 2015), TiO_2 (Qi et al., 2014), MoO_2 (Zhang et al., 2017), conductive polymers (Yilmaz et al., 2017), and metal-organic framework compounds (Sun et al., 2019), which constitute the second-generation

[1]Institute of Industrial and Consumer Product Safety, Chinese Academy of Inspection and Quarantine, Beijing 100176, P. R. China

[2]School of Materials Science & Engineering, Nanyang Technological University, Singapore 639798, Singapore

[3]School of the Environment and Safety Engineering, Jiangsu University, Zhenjiang 212013, P. R. China

[4]Physical Property Measurement Department, Beijing Center for Physical & Chemical Analysis, Beijing 100089, P. R. China

[5]School of Physics and Physical Engineering, Qufu Normal University, Qufu 273165, P. R. China

[6]These authors contributed equally

[7]Lead Contact

*Correspondence: xiguangcheng@caiq.org.cn

https://doi.org/10.1016/j.isci.2019.08.040

of SERS substrates. Interestingly, amorphous semiconductors have recently been found to have better SERS performance than crystalline ones (Wang et al., 2019; Wang et al., 2017; Li et al., 2018a, 2018b). Compared with noble-metal SERS substrates, nanostructural semiconductors possess tailorable band structure and more abundant resonance modes, and therefore can controlled detect target analyte with corresponding excitation-wavelength (532, 633, 785 nm, etc.). In addition to these features, semiconductor SERS substrates also have superior biocompatibility, easy-to-control morphology, and more abundant surface states and active sites. However, for the two most important parameters of SERS, Raman enhancement factors (EFs) and lowest detectable limit of analyte, CM-based semiconducting materials are generally much lower than that of noble metals driven by EM. Furthermore, compared with noble metals, the chemical stability and thermal stability of semiconducting materials are often poor, especially when they are exposed to the excitation light of Raman spectrometer; they are often oxidized or decomposed, thus losing their SERS activity. For example, although $W_{18}O_{49}$ (Cong et al., 2015) and Cu_2O (Lin et al., 2017, 2018) have recently achieved excellent EFs of 10^5–10^6 levels, they are easily oxidized by O_2 in the air, thus unavoidably losing their SERS capability. Therefore, it is an urgent problem to find low-cost non-noble-metal SERS substrate materials with high sensitivity, stability, and large-area signal uniformity for the practical application.

Based on the above-mentioned analysis, we hope to find highly sensitive non-noble-metal SERS active materials and explore whether CM and EM have comparable contributions to their SERS effects. Transition metal oxides often contain abundant family members with different valences (e.g., WO_3, $WO_{2.9}$, $WO_{2.8}$, $WO_{2.72}$, WO_2) (Manthiram and Alivisatos, 2012; Xi et al., 2012a, 2012b). Among them, the high-valence species are often insulators or wide-band-gap semiconductors, whereas the low-valence members often have good conductivity and localized-SPR effects owing to their abundant *d*-orbital free electrons, that is to say, low-valence members often have both certain metallicity and semiconductivity, or quasi-metallicity. It is well known that strong localized SPR and appropriate energy level distribution are the essential conditions for EM and CM enhancements, respectively; therefore, if we can find a quasi-metallic metal oxide that has both strong charge transfer and localized SPR effects as SERS materials, it is possible to obtain high sensitivity due to the combination of EM and CM.

As a very interesting transition metal oxide with intermediate valence state, VO_2 nanostructures have been deeply studied and widely applied in fabrication of intelligent temperature-controlled films and electronic devices with ultralow power consumption due to its magical phase transition of insulator-conductor properties (Qazilbash et al., 2007; Strelcov et al., 2009; Morrison et al., 2014). VO_2 has also recently been reported as a smart glass and high performance battery material (Hao et al., 2018; Li et al., 2019). However, the SERS properties are seldom studied. Herein, we report that quasi-metallic VO_2 nanosheet arrays grown on ordinary glass with 16 cm^2 scale can be used as an effective SERS substrate material with outstanding Raman enhancement effect. As a result of the dual enhancement of EM and CM of the VO_2 substrate, the lowest detectable limit to the typical Raman probe molecule Rhodamine 6G (R6G) on the VO_2 nanosheet arrays can be as low as 10^{-10} M level and the maximum EF is up to 6.7×10^7, which are even compared with the commercialized Au SERS substrates. From the perspective of application and fundamental science, our results demonstrate that quasi-metals can be used as ultrasensitive and stable SERS platforms and reveal that CM and EM both contribute equally to the total SERS performance of quasi-metallic materials.

RESULTS

Selection and Structural Design of SERS Substrate Candidate

As a very interesting transition metal oxide, VO_2 has many crystal structures, such as m-VO_2 (monoclinic), t-VO_2 (triclinic), r-VO_2 (rutile), and a-VO_2 (tetragonal). Among them, m-VO_2 contains a metastable b-VO_2 (bronze phase) (Whittaker et al., 2009). We chose b-VO_2 as the candidate for a new SERS active material because theoretical calculations forecast that this structure has an obvious quasi-metallic feature, which is different from the most studied m-VO_2, which exhibits typical semiconductor characteristics at room temperature. As shown in Figure 1A, the results of simulated density functional theory (DFT) calculations clearly show that b-VO_2 present a definite quasi-metallic characteristic. It can be seen that the calculated band gap is about 1.15 eV. At the same time, the highest occupied states of the b-VO_2 near the Fermi level are composed of V 3d orbitals and O 2p orbitals. Combined with these characteristics, therefore, b-VO_2 can be considered as a typical quasi-metal. Furthermore, the free electron gas distribution, which was achieved by conducting the electron localization functions (ELF) calculation, also suggests that there are non-zero

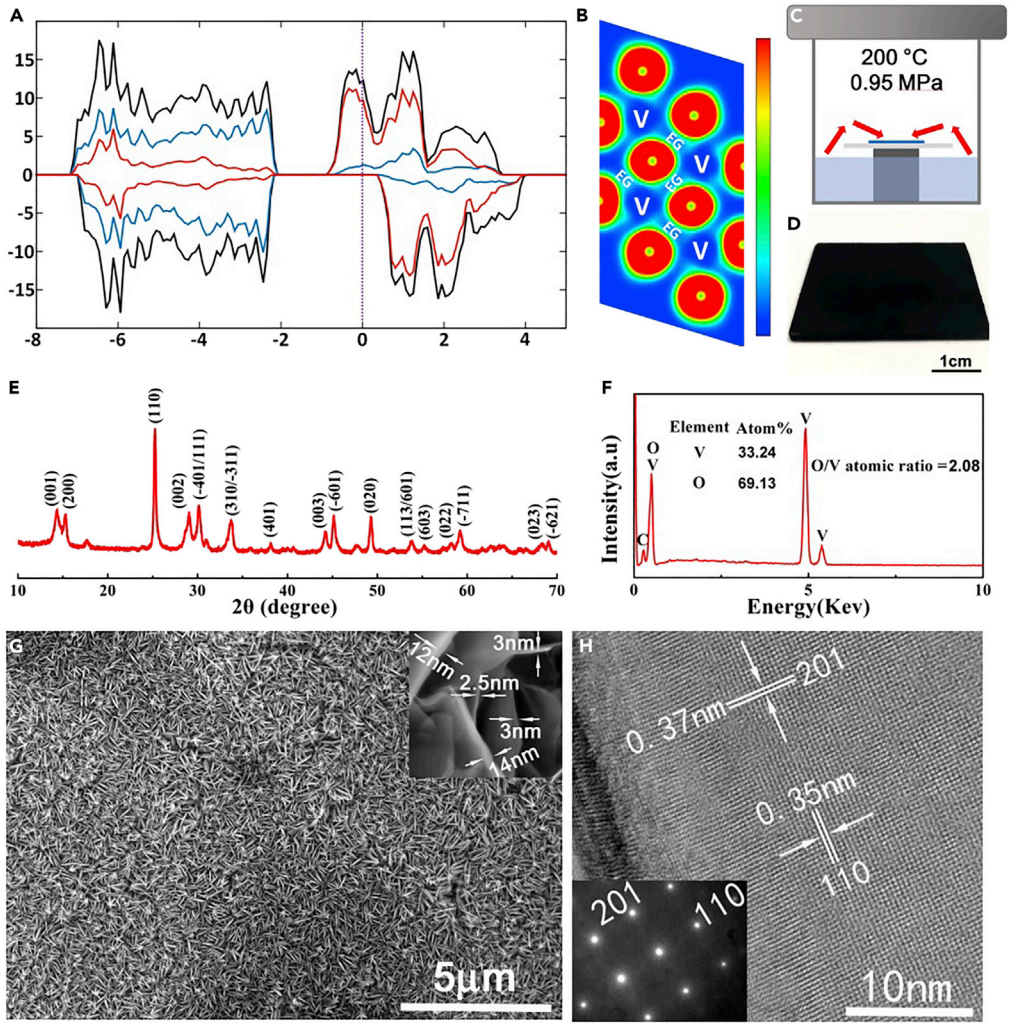

Figure 1. Electric Structures, Synthesis, Crystal Structure, Particle Morphology, and Microstructure of b-VO_2

(A) Electronic density of states for b-VO_2.

(B) The calculated ELF of b-VO_2. Green to red indicates the gradually increased charge localization.

(C) Schematic illustrating the synthesis of the metallic b-VO_2 nanosheet array on glass.

(D) The prepared substrate covered with black b-VO_2 nanosheets.

(E) XRD pattern of the b-VO_2 sample.

(F) EDS component analysis of the b-VO_2 sample.

(G) SEM images of the b-VO_2 nanosheet arrays.

(H) HRTEM image of the b-VO_2 nanosheets, showing the exposed crystal face is (112).

free electron tunnels between V atoms (Figure 1B). These tunnels of free electrons could form non-polar V-V metallic bonds, giving b-VO_2 conducting properties. From the perspective of SERS, the quasi-metal characteristic of b-VO_2 suggests that it may have the synergistic enhancement effect of charge-transfer-induced CM and localized SPR-driven EM.

It is known that charge transfer between analyte and substrate is a short-range action (Park and Kim, 2010);, therefore, the enhancement effect based on CM is closely related to the scale and dimension of substrate materials. Recent studies on two-dimensional (2D) SERS active materials such as graphene and molybdenum disulfide nanosheets show that effective charge transfer between the adsorbed molecules and the substrates requires that the surface of the material be as flat as possible to effectively adsorb the molecules to be measured (Xie et al., 2009; Muehlethaler et al., 2016). At the same time, to obtain strong interactions of analytes and substrates, the thickness of these SERS active materials should be as small as possible to

minimize the loss of charge carriers during the transfer process (Li et al., 2018a, 2018b). On the other hand, the localized-SPR-based EM enhancement generally requires that the surface of the SERS substrate be as rough as possible, preferably containing a large number of nano-scale gaps, to generate a large number of high-intensity electromagnetic "hot spots" (Willets, 2014). From these two seemingly contradictory aspects, we expect to synthesize b-VO_2 ultrathin nanosheet arrays, which not only meets the structural requirements of charge transfer, but also satisfies the demand of forming a large number of high-intensity electromagnetic "hot spots" among the nanosheet gaps.

Synthesis and Characterizations of VO_2 Nanosheet Arrays

According to the previous analysis, a facile, scalable, and low-cost hydrothermal-assisted chemical vapor decomposition (HCVD) route has been designed for the *in situ* growth of the large-area b-VO_2 ultrathin nanosheet arrays on glass (16 cm^2 level). As shown in Figure 1C, an appropriate amount of vanadyl acetylacetonate (VAA) is dissolved in a certain volume of absolute ethanol to form a bright blue transparent solution. The resulting homogeneous solution is then transferred to a Teflon-lined high-pressure reactor, and a common glass sheet is placed above the liquid level as a growth platform for b-VO_2 nanosheets. At 200°C, the closed reaction system is filled with ethanol vapor mixed with VAA molecules. Under this solvothermal condition, these tetravalent vanadium atoms contained in VAA will undergo alcoholysis to form crystal clusters of VO_2, which are then deposited on glass surface and grown into arrayed nanosheets. The key to the success of this method is to maintain a reductive reaction atmosphere in the autoclave; otherwise it is very easy to generate V_2O_5 with a higher valence state. In the reactor, ethanol vapor exactly has a considerable strong reducibility under the heating conditions. Contrast experiments show that, if ethanol is replaced by deionized water, the obtained product is V_2O_5 nanobelts (Figure S1). As shown in Figure 1D, a glass sheet of 4 cm × 4 cm can be completely covered by a layer of black b-VO_2 nanosheets after 12 h of HCVD reaction, which suggests that our method is very suitable for the growing of large-area VO_2 nanosheet arrays.

The crystal phase of the obtained product was determined by X-ray diffraction (XRD) technology. The XRD pattern of the black sample can be accurately indexed as the monoclinic b-VO_2 with the lattice parameters of a = 4.5968, b = 5.6844, c = 4.9133, and β = 89.398° (JCPDF No. 65-7960), and no other crystalline phase was found (Figure 1E). Energy dispersive spectrum (EDS) reveals that these samples contain only V and O elements, and the O/V ratio is about 2.08, which further proves that this sample is indeed VO_2 (Figure 1F). The morphology and crystallographic orientation of the sample were investigated by field-emission scanning electron microscopy (SEM) and high-resolution transmission electron microscope (HRTEM). Overall, the black products are a lay of very uniform sheet-like nanostructures, which are vertically distributed on the glass surface (Figure 1G). High-magnification SEM images show that the thickness of these b-VO_2 nanosheets are only 3–15 nm (inset in Figure 1G). Interestingly, there are many thin nanosheets interspersed between these thick nanosheets, a feature that is very helpful to adsorb more molecules on the surfaces and strongly promote charge transfer between nanosheets and analytes. Furthermore, the clear lattice fringes recorded in the HRTEM image demonstrate that these b-VO_2 nanosheets possess a high crystallinity (Figure 1H). The lattice fringes with the interplanar spacing of 0.37 and 0.35 nm can be accurately referred to as the (201) and (110) crystal faces, respectively, which are also confirmed by the corresponding selected area electron diffraction pattern (inset in Figure 1H). Based on the information of the HRTEM image, it can be reasonably calculated that the exposed crystal face of the nanosheets is (112). Interestingly, this exposed crystal surface can interact strongly with the probe molecule R6G of SERS, which will be further demonstrated below. The specific BET (Brunauer-Emmett-Teller) surface area of the b-VO_2 nanosheets was determined to be 44.8 $m^2\ g^{-1}$ (Figure S2). In addition, Fourier transform infrared spectroscopy and Raman spectroscopy characterizations suggest that the surfaces of these nanosheets are very clean (Figures S3 and S4) and there was no signal of reaction residues except b-VO_2, which is very important for trace detection because it can reduce the interference of the substrate itself.

Localized SPR Effect and Stability

X-ray photoelectron spectroscopy (XPS) was used to identify the binding states and chemical compositions of these b-VO_2 nanosheets. The XPS survey spectrum shows that these detected peaks at 515.2 and 631.3 eV can be identified as V 2p and V 2s of V^{4+}, respectively (Figure 2A), which is characteristic of vanadium dioxide (Nethravathi et al., 2013). The peak at 529.6 eV can be assigned to O 1s of the O^{2-}. The high-resolution XPS of V 2p, as shown in Figure 2B, could be well fitted into two spin-orbit doublets, corresponding to V^{4+} and V^{5+} oxidation states, respectively. The two characteristic strong peaks at 516.03 and 523.35 eV can be indexed to V^{4+}, whereas the other two weak shoulder peaks at 517.38 and 524.61 eV can be

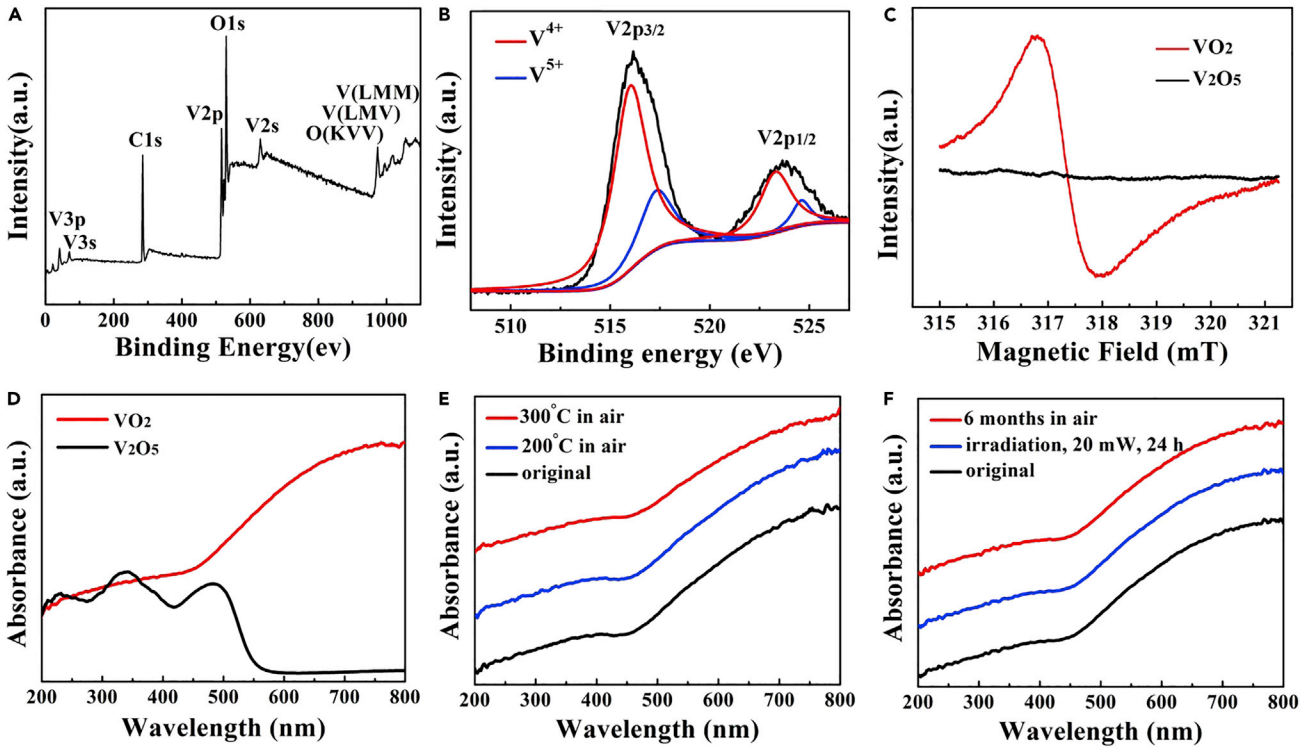

Figure 2. Valence States, EPR, and Ultraviolet-vis Absorption Characterizations of the b-VO_2 Nanosheets

(A) XPS survey spectrum of the b-VO2 nanosheets.

(B) V 2p spectrum of the b-VO_2 nanosheets, which demonstrates that most vanadium ion in the sample is tetravalent.

(C) EPR spectrum of the sample, displaying a strong free electron signal.

(D) Ultraviolet-vis absorption spectrum of the sample, showing a strong LSPR absorption from visible to NIR regions.

(E and F) The LSPR absorption of these samples are almost the same after being heated in air (E) and irradiated by laser and long-term preservation in air (F), suggesting the high thermal and chemical stability of the metallic b-VO_2 nanosheets.

attributed to V^{5+}. According to the size of the peak areas, the concentration of V^{4+} on the sample surface is much higher than that of V^{5+}, which confirms that the vanadium ion in the sample is basically tetravalent. At the same time, the strong electron paramagnetic resonance (EPR) spectrum signal directly demonstrated that the b-VO_2 nanosheets have a large number of free electrons in its *d*-orbital (Figure 2C). In contrast, V_2O_5 nanosheets (morphology see Figure S5) obtained by oxidizing the VO_2 nanosheets at 400°C in air were not detected by the effective ESR signals. These XPS and EPR results are highly consistent with the theoretical results mentioned earlier, which together prove that these b-VO_2 nanosheets contain a high concentration of *d*-orbital free electrons.

Importantly, these abundant *d*-orbital free electrons make the b-VO_2 nanosheets exhibit strong localized-SPR effect from visible to near-infrared (NIR) regions (Figure 2D), which provides the possibility for EM enhancement of SERS to take place. In contrast, V_2O_5 nanosheets without free d-orbit electrons did not exhibit SPR behavior. Many intermediate valence transition metal oxide nanomaterials with strong localized-SPR are easy to be oxidized by oxygen in air, thus losing the SPR behavior and the corresponding SERS activities, which is another major obstacle to the practical application of semiconductor SERS substrates in addition to their low sensitivity. For example, plasmonic $W_{18}O_{49}$ nanostructure has been reported to have excellent SERS performance, and its Raman EF (10^5) is comparable with that of noble metals. However, for $W_{18}O_{49}$, even if heated at 100°C for 5 h in air, its SPR activity quickly disappears owing to oxidation (Figures S6 and S7). In contrast, the b-VO_2 nanosheets show a high oxidation resistance (Figure 2E). Even if heated at 300°C in air for 1 h, the intensity and position of the plasma resonance absorption of these nanosheets did not change significantly, which is rare in transition metal oxides with intermediate valence states. This strong oxidation resistance has also been demonstrated by its high thermal stability (Figure S8). Considering that SERS substrates are exposed to the laser irradiation of Raman spectrometer, the high

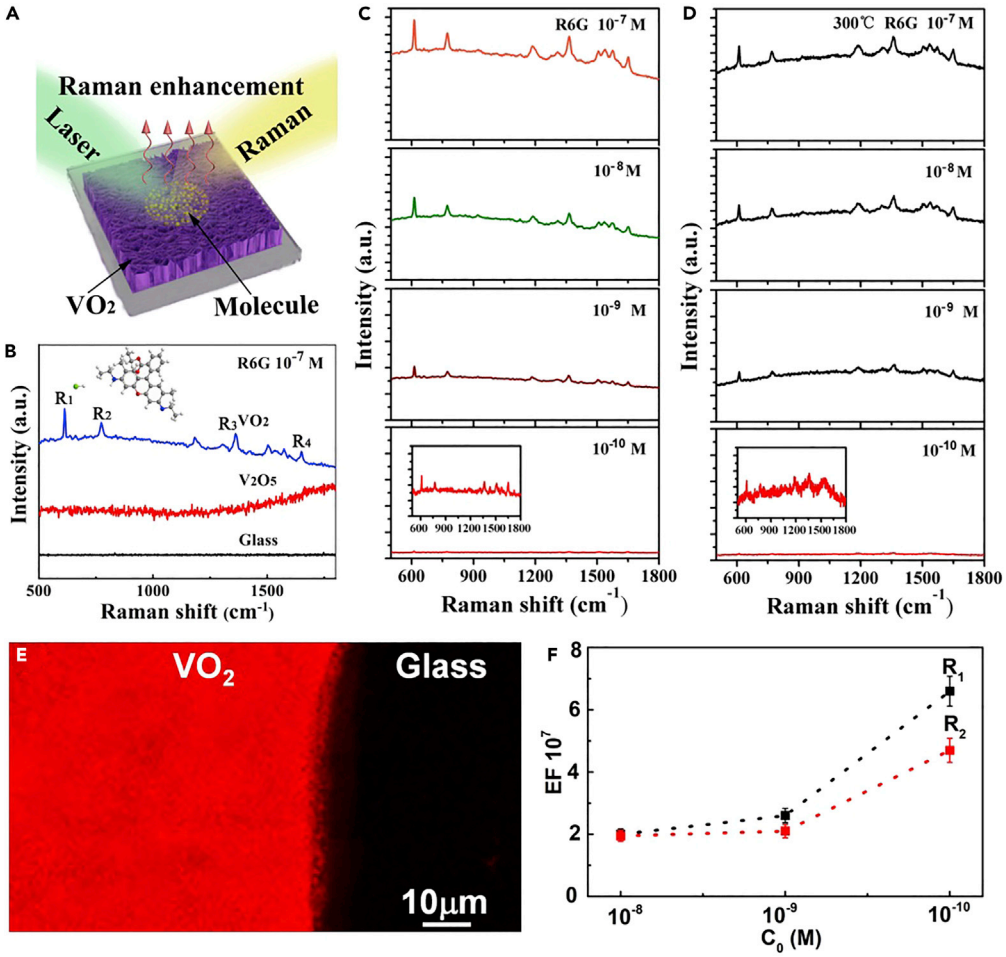

Figure 3. SERS Measurements of R6G with the as-Prepared b-VO_2 Nanosheets

(A) SERS measurement schematic diagram.

(B) Raman spectra of 10^{-7} M R6G aqueous solution obtained on b-VO_2 nanosheets, bare glass, and V_2O_5 nanosheets.

(C) Gradually weakened Raman scattering signals recorded from Rh6G aqueous solution at four different concentration levels (10^{-7}, 10^{-8}, 10^{-9}, 10^{-10} M), suggesting that the b-VO_2 nanosheets have greatly enhanced Raman scattering, with a lowest detection limit of 10^{-10} M for analytes.

(D) These b-VO_2 nanosheets still have high Raman enhancement effects even after 300°C of high-temperature heating in air.

(E) SERS mapping near an edge of a R6G/b-VO_2 film.

(F) The average Raman EFs obtained by counting the peak intensities (R_1 and R_2) at three different concentration levels.

stability of the substrate materials is extremely important. In addition to the strong oxidation resistance, these b-VO_2 nanosheets also exhibit long-term environmental and irradiated stability (Figure 2F). Even after exposure to air for 6 months, their SPR peaks did not change noticeably, which provides an opportunity for the commercialization of this material. The stability of these b-VO_2 nanosheets was also confirmed by XRD and XPS characterization (Figures S9 and S10).

Enhanced Raman Scattering

Then, we tested the SERS properties of the b-VO_2 nanosheet array substrate. As shown in Figure 3A, in all SERS measurements, the Raman exciting light is incident from above the substrate plane. In the experiments, the prepared probe molecule (R6G) solutions with specific concentrations (10^{-7}–10^{-10} M) was added dropwise into the b-VO_2 nanosheet arrays and dried at room temperature for 10 min before SERS measurement (see the Transparent Methods section for the specific process). Figure 3B shows that the b-VO_2 nanosheet arrays exhibit excellent SERS activity for R6G with a concentration of 10^{-7} M (blue spectrum in Figure 3B). All Raman scattering peaks

are clearly visible and highly consistent with the standard Raman spectrum of R6G reference material (Figure S11). The strongest four Raman scattering peaks at 612 (R_1), 773 (R_2), 1,363 (R_3), and 1,652 cm^{-1} (R_4) can be clearly observed, in which R_1 and R_2 can be indexed with the in-plane and out-of-plane bending motions of C and H atoms of the xanthenes skeleton, respectively; R_3 and R_4 can be referred to the C-C stretching vibrations of aromatic nucleus (Hildebrandt and Stockburger, 1984). To eliminate the contribution of glass to the properties of SERS since the nanosheets are grown on them, the R6G probe solutions were directly dripped onto the bare glass and tested for Raman signals. The results showed that no Raman signals were detected (black spectrum in Figure 3B), which definitely excludes the contribution of the glass in the SERS. When the quasi-metallic b-VO_2 nanosheets were completely oxidized to the semiconducting V_2O_5 nanosheets without localized SPR effect (Figure S5), no effective SERS signals of probe molecules was detected except for the fluorescence background (red spectrum in Figure 3B), which further confirms that the enhanced Raman signals come from the quasi-metallic B-VO_2 nanosheet arrays. On the other hand, contrastive experiments revealed that the bare b-VO_2 nanosheet arrays without R6G solution only showed the typical Raman scattering peaks of themselves (Figure S12), indicating the enhanced Raman scattering peaks represented by R_1, R_2, R_3, and R_4 really originate from R6G molecules.

Figure 3C shows the SERS spectra of a series of R6G samples with different concentrations (10^{-7}, 10^{-8}, 10^{-9}, 10^{-10} M). It can be seen that the b-VO_2 substrate exhibits excellent SERS performance in a large concentration range. Even when the concentration of R6G is only 10^{-10} M, the distinguishable Raman signals still can be detected (signal-to-noise ratio greater than 5). Such a low detection limit allows this new SERS substrate to be used to trace even single-molecule detection of compounds with ultrahigh sensitivity. More importantly, this new SERS substrate based on the b-VO_2 nanosheets has considerable high stability. As mentioned earlier, these b-VO_2 nanosheets will not lose their localized-SPR effect even if heated at 300°C in air; accordingly, after the b-VO_2 nanosheets were treated at 300°C for 5 h, it can be seen that their SERS intensities did not decrease noticeably and even 10^{-10} M analytes could still be detected (Figure 3D). For the practical applications of SERS, high stability of the SERS substrates is very important, because when transition metal oxides-based SERS substrates with intermediate valence state are exposed to the laser irradiation of Raman spectroscopy, they could often easily be oxidized or deformed, thus losing SERS activity or the reproducibility of the signals.

Raman scattering EF is generally considered to be the most important factor in evaluating the performances of SERS substrates. To visualize the EF of the VO_2 nanosheet arrays, Figure 3E shows the Raman mapping image recorded from the edge of a R6G/VO_2 layer. The obtained Raman mapping is clearly separated into two regions: the area covered with VO_2 nanosheets showed strong Raman signals of R6G, whereas the R6G directly placed on the glass did not show any signals, suggesting the high uniform and strong SERS enhancement originated from the densely arranged VO_2 nanosheets. To evaluate the Raman EF of the VO_2 nanosheets more accurately, control experiments were carried out. In these experiments, on the VO_2 nanosheet arrays, the SERS signal intensity of R_1 and R_2 scattering peaks of R6G with 10^{-8}, 10^{-9}, and 10^{-10} M was measured (integration time is 10 s). As references, on the bare glass, the normal Raman signal intensity of R_1 and R_2 scattering peaks of R6G with a much higher concentration (10^{-2} M) and integration time (4,000 s) was also measured under the same excitation light and operating mode. The calculated maximum EF is more than 6.7×10^7 (Figure 3F), which can be compared with the EFs of noble-metal substrates and is sufficient for single-molecule detection. As far as we know, the EF and detection limit of the quasi-metallic b-VO_2 nanosheet arrays in various reported non-noble-metal SERS substrates (Table S1) are only lower than that of Mo(W)Te_2 nanosheets with atomic layer thickness (Li et al., 2018a, 2018b). But considering the difficulty of synthesis and quality control of the Mo(W)Te_2 monatomic layers, these large-scale VO_2 SERS substrates, which are easy to synthesize, have great advantages in practical applications.

Uniformity and Repeatability of SERS Signals

In addition to the high sensitivity and EF, the large-range homogeneity and reproducibility of Raman signals is another important index to evaluate the performance and practicability of SERS substrate. The premise of obtaining uniform and repeatable signals is the uniformity of the substrate surface. As shown in Figure 4A, the optical photographs of one glass sheet covered with b-VO_2 nanosheets show that the surface of the substrate is very uniform, which is highly consistent with the SEM characterizations described earlier. In the area shown in Figure 4A, 100 points are selected randomly for SERS detection, and the results show that the Raman spectra obtained by these points are highly consistent (Figure 4B), indicating that the present SERS substrate has excellent signal uniformity and reproducibility. The Raman mapping result of R_1 scattering peak at 612 cm^{-1} recorded from 5,000 measuring points displays a uniform intensity distribution

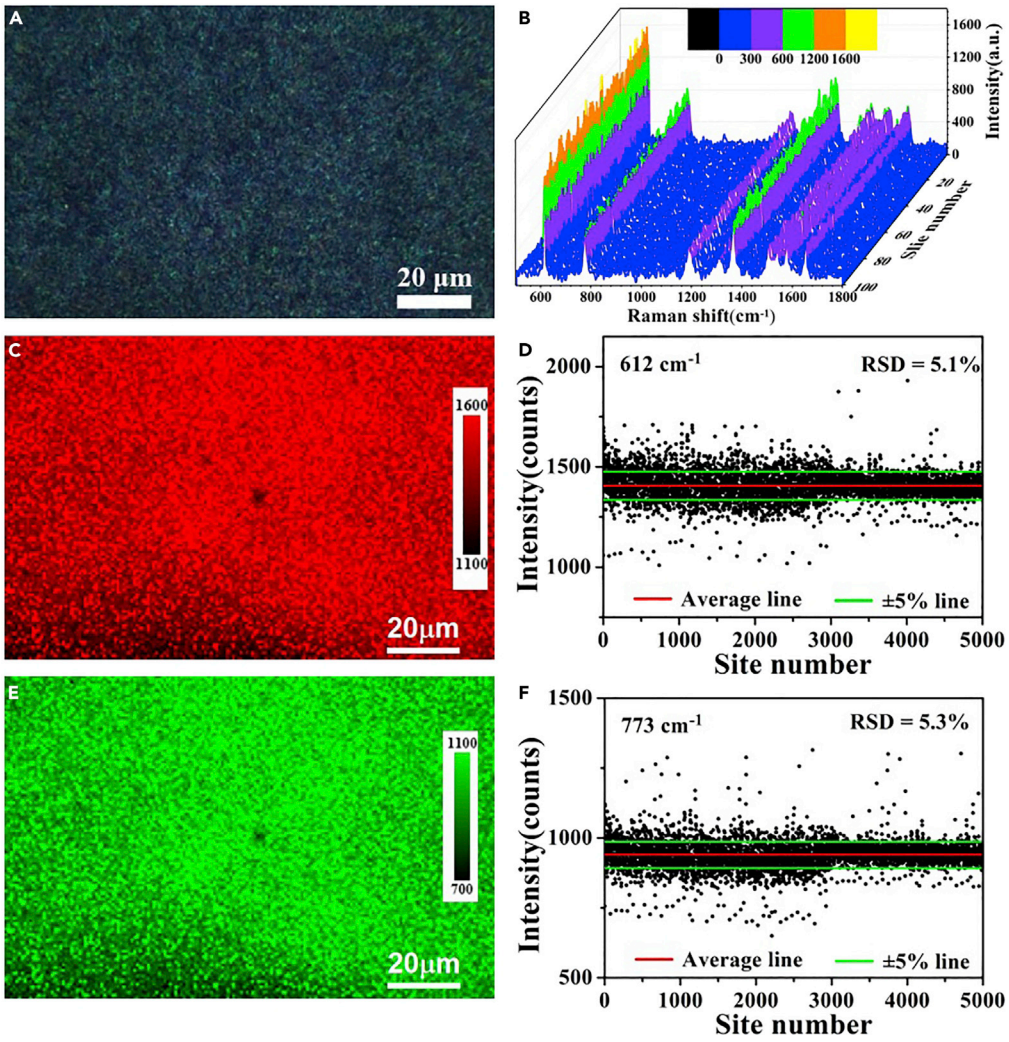

Figure 4. Determination of the Signal Reproducibility and Uniformity of the Metallic b-VO_2 Nanosheet Substrate

(A) Optical photograph of the substrate covered with b-VO_2 nanosheets recorded from objective lenses of the Raman spectrometer.

(B) SERS signals collected from 100 randomly selected measuring points on the substrate.

(C) The SERS mapping at 612 cm^{-1} (R_1) of 10^{-8} M R6G in the region shown in Figure 4A.

(D) The signal intensities at 612 cm^{-1} (R_1) of 10^{-8} M R6G in the region shown in Figure 4A.

(E) The SERS mapping at 773 cm^{-1} (R_2) of 10^{-8} M R6G in the region shown in Figure 4A.

(F) The SERS signal intensities at 773 cm^{-1} (R_2) of 10^{-8} M R6G in the region shown in Figure 4A.

(Figure 4C), which further confirms the signal uniformity of the substrate in large scale. By counting the distribution of the intensity values of the 5,000 R_1 peaks, the acquired relative standard deviation (RSD) is only 5.1% (Figure 4D). Similarly, the Raman mapping and statistical results of R_2 scattering peak at 773 cm^{-1} also demonstrated the high signal uniformity of the b-VO_2 substrate (Figure 4E), with RSD of about 5.3% (Figure 4F). Such high signal reproducibility makes it possible for the practical application of this new SERS substrate.

Universality as SERS Detection Platform

In addition to exhibiting the high sensitivity for the probe molecule of R6G, this quasi-metallic b-VO_2 SERS substrate also exhibits very low detection limits for several other common dye molecules, such as methyl blue, methyl orange, and Rhodamine B. From 10^{-8} to 10^{-10} M, the resolvable Raman signals of the dye molecules can be measured from the nanosheet arrays (Figures 5A and S13). More importantly, the quasi-metallic VO_2 substrate also exhibits excellent sensitivity to a range of highly concerned risk

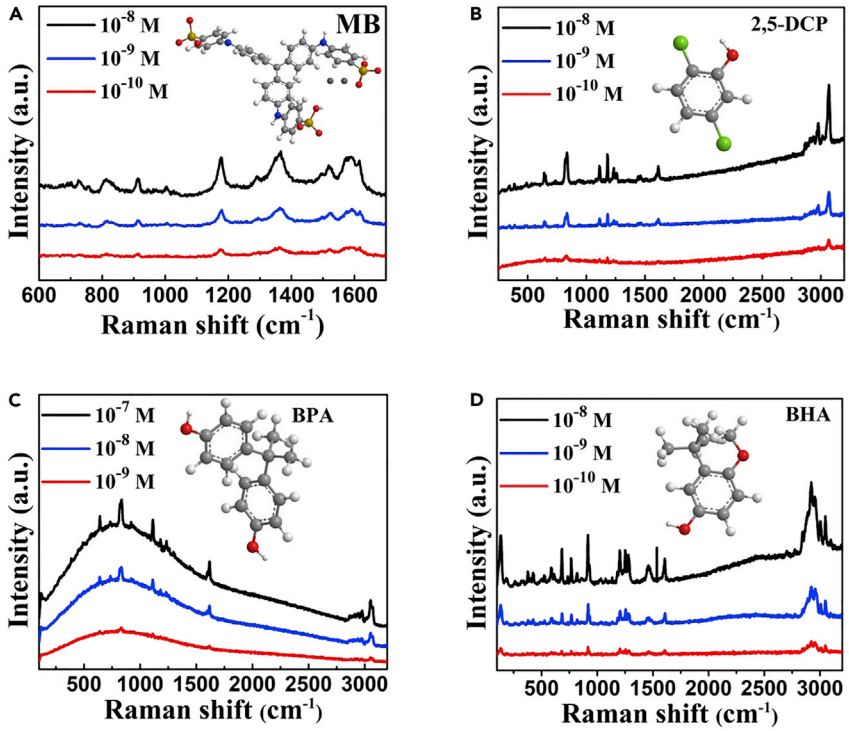

Figure 5. SERS Spectra of a Series of Common Environmental Pollutants

(A) Methyl blue (MB).

(B) 2,5-Dichlorophenol (2,5-DCP).

(C) Bisphenol A (BPA).

(D) Butyl hydroxy anisd (BHA).

substances. Dichlorophenol, a common environmental hormone, has been proved to be highly carcinogenic and has attracted much attention from environmental monitoring departments in various countries. On this b-VO_2 nanosheet arrays, the 2,5-dichlorophenol (2,5-DCP) molecules can be sensitively detected even if its concentration is only 10^{-10} M (Figure 5B). Another hazardous environmental hormone, bisphenol A (BPA), has been banned in the United States, the European Union, Canada, China, and so on. It is reported that BPA is an endocrine disruptor, which can mimic human hormones and may lead to adverse health effects. Like 2,5-DCP, BPA also can be sensitively detected at 10^{-10} M level on the b-VO_2-based SERS substrate (Figure 5C). In addition, as a powerful antioxidant, butyl hydroxy anisd (BHA) has long been used to prevent food spoilage. However, recent studies have shown that it may have strong carcinogenicity and has been banned from food industry in Japan, China, and other countries. It is found that this VO_2 SERS substrate also responds well to BHA (Figure 5D). These experimental results showed that the quasi-metallic b-VO_2 nanosheet arrays are a versatile SERS active substrate to a series of chemicals.

Raman Enhancement Mechanism of the Quasi-Metallic VO_2

Traditionally, the Raman enhancement of noble-metal SERS materials can be explained by EM based on the well-known localized-SPR effect, whereas the enhancement of semiconductor SERS materials can be attributed to the CM resulting from the charge transfer between the adsorbed molecules and the substrates (Li et al., 2010; Qian et al., 2008). Although it is now accepted that both enhancement mechanisms may take place together in one substrate, it is generally believed that the enhancement effect of CM is far less than that of EM owing to the short-range effectiveness of CM. However, our present research results break this traditional view, revealing that CM, like EM, also plays an important role in the enhancement of the total SERS performances when the substrate is quasi-metal. First, UV-vis absorption spectra are to used to examine whether there is charge transfer between the analyte molecule and the VO_2 nanosheets. We measured the absorption spectra of pure R6G solution, clean VO_2 nanosheets, and VO_2 nanosheets adsorbed with R6G molecules, respectively. As shown in Figure 6A, compared with those of the pure R6G,

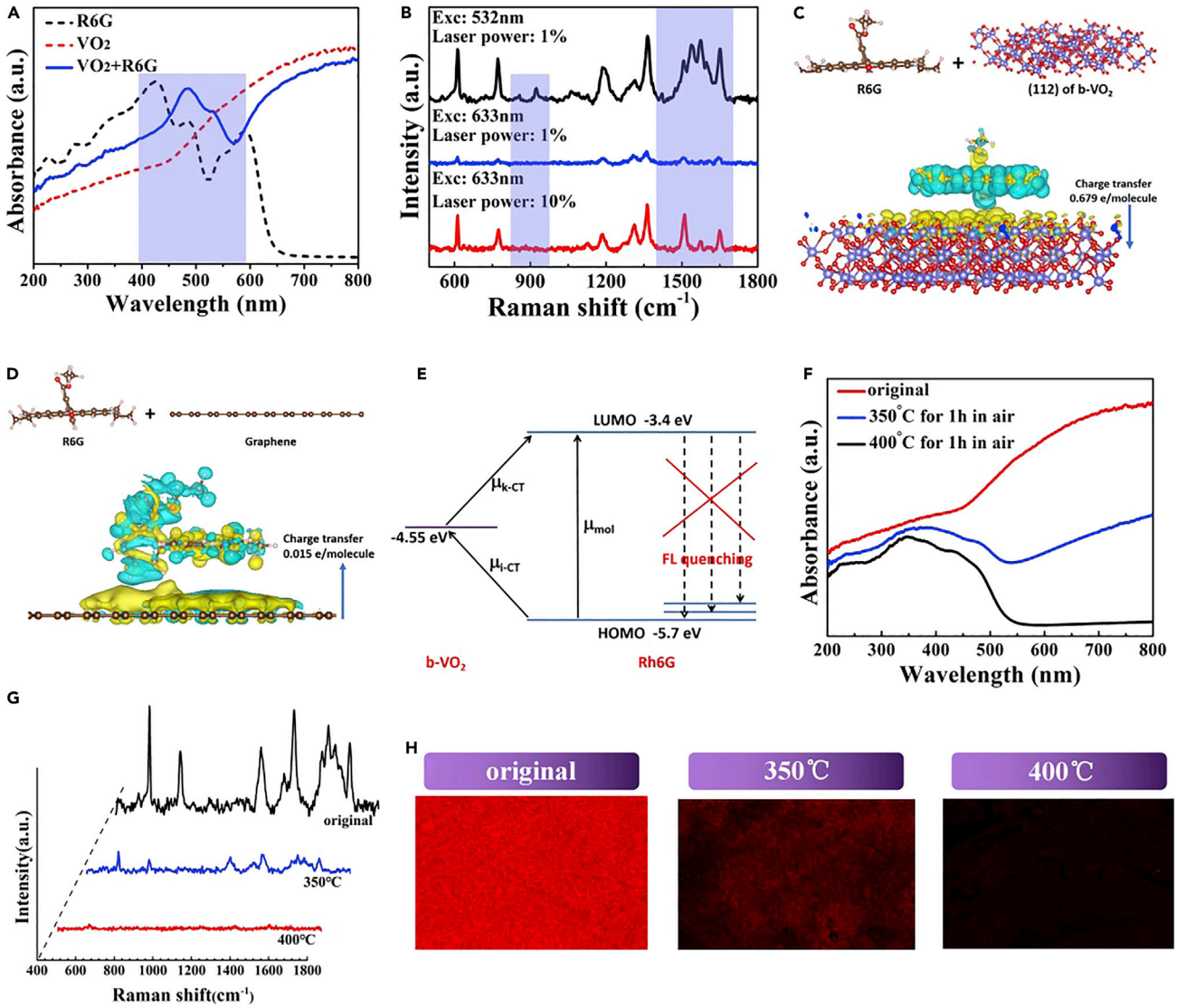

Figure 6. Investigation of the Enhanced Mechanism of the b-VO_2 Nanosheet Substrate

(A) Absorption spectra for R6G on VO_2 compared with neat VO_2 and R6G dye. The colored area denotes the R6G absorption band on VO_2.

(B) Changing excitation wavelength has a great influence on SERS intensity and resonance mode.

(C and D) Side views of the electron density difference isosurfaces for R6G chemisorbed onto the (112) crystal face of b-VO_2 (C) and graphene (D). Blue and yellow colors correspond to electron depletion and accumulation regions, respectively. The arrows indicate the direction of electron transfer.

(E) Energy level diagram and charge transfer transitions in the R6G-VO_2 complex. μ_{mol} denotes the molecular transition. $\mu_{i\text{-}CT}$ and $\mu_{k\text{-}CT}$ denote the charge transfer transitions from the molecular ground states to VO_2 and from VO_2 to the molecular excited states, respectively.

(F) UV-vis absorption spectra of the vanadium oxide samples obtained by oxidation for different time periods.

(G) SERS spectra recorded from the vanadium oxide samples with different SPR effects, respectively.

(H) SERS mapping over the vanadium oxide samples with different SPR effects, respectively.

the main absorption peaks of R6G adsorbed on VO_2 nanosheets took place at a significant redshift (marked with color bar), suggesting the strong interaction and charge transfer probability between R6G and VO_2. SERS based on CM is very sensitive to the wavelength changes of exciting light, and lasers of different wavelengths often lead to different molecular vibration modes, which are typical characteristics of CM enhancement. As shown in Figure 6B, the experimental results showed that the intensity of Raman scattering signals of R6G decreases obviously when the wavelength of exciting light changes from 532 to 633 nm, which can be reasonably attributed to the fact that the energy of 633-nm exciting light is obviously less than that of 532 nm. When the exciting power is increased by 20 times (633 nm), the Raman signal

intensity of R6G is obviously increased, but it should be pointed out that the resonance mode of R6G molecule has significantly changed in several bands (marked with color bars), which further proves that there is a strong interaction between the analyte and the substrate. It was noted that, when graphene was used as the SERS substrate (its SERS activity has been reported [Xie et al., 2009]), only its own Raman signals have been detected and no effective Raman signals of R6G were detected (Figure S14), which indicated that the charge transfer between VO_2 nanosheets and R6G is much larger than that between graphene and R6G. This phenomenon may be attributed to the chemical inertness of the graphene surface, whereas the surface of quasi-metal nanosheets synthesized by the solution method is much more active.

The interactions between the adsorbed R6G molecules and the VO_2 nanosheets and subsequent charge transfer were investigated by DFT simulation (Figures 6C and 6D). The DFT calculations revealed that the binding energy of R6G and VO_2 with exposed (112) crystal plane is 1.15 eV, whereas the binding energy of R6G and graphene is only 0.67 eV. At the same time, the results also show that the electron transfer from R6G to VO_2 is 0.679 e/molecule, whereas that for graphene and R6G is only 0.015 e/molecule (from graphene to R6G). The obvious difference in the values of the binding energy and electron transfer demonstrated that the coupling effect of VO_2 and R6G is much stronger than that of graphene and R6G. At the same time, from the charge density isosurfaces, the DFT simulations also showed that the electrons and holes generated by charge transfer form a strong dipole at the interface of R6G and VO_2, which would strengthen the Raman scattering of R6G molecules on VO_2 nanosheets. As a contrast, the forming dipole between VO_2 and R6G is much stronger than that of graphene and R6G owing to the greater charge transfer, which further proves the strong coupling effect between VO_2 and R6G. Furthermore, owing to the relatively high surface activity of VO_2 nanosheets, the generated charge carriers are concentrated at the interface of VO_2 and R6G, forming so-called quasi-covalent bonds (Li et al., 2018a, 2018b), which would further enhance the coupling of VO_2 and R6G in addition to the electrostatic force of dipole. Thus, the strong dipole effect and the consequent quasi-covalent bonds lead to the impressive SERS capability of the quasi-metallic VO_2 nanosheets together.

In addition to the CM induced by the electrostatic coupling between R6G and VO_2 discussed earlier, the outstanding SERS performance of the VO_2 substrate also can be attributed to the photo-induced charge transfer (PICT) caused CM, as shown in Figure 6E. The energy levels of the highest occupied molecule orbital (HOMO) and the lowest occupied molecule orbital (LOMO) of R6G are −5.7 and −3.4 eV, respectively (Hildebrandt and Stockburger, 1984), whereas the Fermi level of b-VO_2 nanosheets is 4.55 eV according to the characterization results of Kelvin probe force microscope as illustrated in Figure S15. The distribution of the levels is allowed to both the PICT transfer from the HOMO of R6G to the Fermi level of b-VO_2, and the Fermi level of VO_2 to the LOMO of R6G, which are beneficial to the SERS due to the wide energy range of charge transfer resonance. Therefore, the resonances greatly enhance the polarization tensor of the R6G molecule according to the well-known Herzberg-Teller vibronic coupling (Lombardi et al., 1986). It should be noted that the Fermi level of VO_2 is almost a symmetrical match to the HOMO and LUMO of R6G (Figure 6E), which further promotes the PICT process, and the interference of fluorescence background of R6G is greatly reduced.

In addition to the CM-based Raman enhancement mentioned earlier, EM enhancement also contributes significantly to the overall SERS performances of the quasi-metallic VO_2 substrate. As illustrated in Figure S16, when these VO_2 nanosheets were heated in air for a period of time, their colors changed dramatically. Accordingly, their plasma resonance absorption significantly reduced and ultimately became imperceptible (Figure 6F). Obviously, this is because the VO_2 sample is gradually oxidized to V_2O_5 (Figures S17 and S18), thus losing a large number of *d*-orbital free electrons, and correspondingly its localized SPR is also weakened and eventually disappeared. As a direct result, the SERS performance of these oxidized samples is greatly reduced (Figure 6G). The Raman mapping results also show that the SERS effect of the sample weakens with the decrease of the SPR intensity (Figure 6H). On the contrary, when we increase the concentration of oxygen vacancies in the VO_2 nanosheets by the chemical reduction method (by immersing the VO_2 sample in strongly reducing $NaBH_4$ aqueous solution), the corresponding SPR absorption increases gradually (Figure S19) and the corresponding SERS signal also increases gradually (Figure S20). Based on the results, we believe that the regular relationship between the localized-SPR strength and the corresponding SERS performance demonstrated that EM enhancement also exists in the quasi-metallic b-VO_2-based SERS. To further prove the existence of EM, these nanosheets are coated with amorphous SiO_2 (named as SiO_2/VO_2) to block charge-transfer-based CM enhancement by an ingenious synthesis experiment (Figure S21). Compared with bare VO_2 nanosheets, the SERS signal intensity of analyte on the VO_2/SiO_2 still can be detected, as shown in (Figure S22), which undoubtedly proves the existence of

EM. Conversely, this result also further verified the existence of CM. For the total Raman enhancement, by calculating the peak area of R_1 recorded on VO_2 and VO_2/SiO_2, respectively, it can be concluded that the contributions of CM and EM are about 57% and 43%, respectively, which revels that both CM and EM play an important role in enhancing the Raman scattering.

Conclusions

In summary, we demonstrate that quasi-metallic b-VO_2 nanosheet arrays can be used as a highly sensitive and stable SERS substrate material. The lowest detectable limit of R6G probe on the VO_2 substrate can achieve picomole levels and the optimal Raman EF is up to 6.7×10^7, which obviously outstrips the previously reported CM based solely on SERS active materials represented by semiconducting nanostructures, graphene, metal organic frameworks, and so on. The ultrasensitive SERS performances achieved on the quasi-metallic VO_2 nanosheet arrays can be attributed to the strong analyte-substrate interactions and the vigorous localized-SPR effects of the VO_2. The present research results indicate that the quasi-metallic VO_2 nanosheet array is a very promising SERS detection platform and demonstrates that CM and EM together play a key role in the overall SERS performance of quasi-metals.

Limitations of the Study

At present, it is difficult to accurately evaluate the contributions of EM and CM in quasi-metal. Although we use a thin layer of amorphous SiO_2 to isolate charge transfer, it may also affect EM and introduce new interface effects. A more perfect evaluation method needs to be established in the future to accurately identify the contribution of EM and CM to the properties of quasi-metal SERS.

METHODS

All methods can be found in the accompanying Transparent Methods supplemental file.

SUPPLEMENTAL INFORMATION

Supplemental Information can be found online at https://doi.org/10.1016/j.isci.2019.08.040.

ACKNOWLEDGMENTS

This work received financial support from the Science Foundation of Chinese Academy of Inspection and Quarantine (2019JK004) and the National Key Research and Development Program of China (2017YFF0210003).

AUTHOR CONTRIBUTIONS

Conceptualization, G.X., Z.T.; Investigation, Z.T., H.B., Y.Y., Q.K., Y.L., and W.F.; Calculation, C.C., and W.Y.; Writing – Original Draft, Z.T. and G.X.; Writing – Review & Editing, Z.T., H.B., and G.X.

DECLARATION OF INTERESTS

The authors declare no competing interests.

Received: June 19, 2019
Revised: August 17, 2019
Accepted: August 21, 2019
Published: September 27, 2019

REFERENCES

Alvarez-Puebla, R.A., and Liz-Marzan, L.M. (2012). SERS detection of small inorganic molecules and ions. Angew. Chem. Int. Ed. *51*, 11214–11223.

Cong, S., Yuan1, Y.Y., Chen, Z.G., Hou, J.Y., Yang, M., Su, Y.L., Zhang, Y.Y., Li, L., Li, Q.W., Geng, F.X., and Zhao, Z.G. (2015). Noble metal-comparable SERS enhancement from semiconducting metal oxides by making oxygen vacancies. Nat. Commun. *6*, 7800.

Fleischmann, M., Hendra, P.J., and McQuillan, A.J. (1974). Raman spectra of pyridine adsorbed at a silver electrode. Chem. Phys. Lett. *26*, 163–166.

Hao, Q., Li, W., Xu, H.Y., Wang, J.W., Yin, Y., Wang, H.Y., Ma, L.B., Ma, F., Jiang, X.C., Schmidt, O.G., et al. (2018). VO_2/TiN plasmonic thermochromic smart coatings for room-temperature applications. Adv. Mater. *30*, 1705421.

Hildebrandt, P., and Stockburger, M. (1984). Surface-enhanced resonance Raman spectroscopy of Rhodamine 6G adsorbed on colloidal silver. J. Phys. Chem. *88*, 5935–5944.

Jeanmaire, D.L., and Van Duyne, R.P. (1977). Surface Raman spectroelectrochemistry. part I. heterocyclic, aromatic, and aliphatic amines adsorbed on the anodized silver electrode. J. Electroanal. Chem. *84*, 1–20.

Kanipe, K.N., Chidester, P.P.F., Stucky, G.D., and Moskovits, M. (2016). Large format surface-enhanced Raman spectroscopy substrate optimized for enhancement and uniformity. ACS Nano *10*, 7566–7571.

Kneipp, K., Wang, Y., Kneipp, H., Perelman, L.T., Itzkan, I., Dasari, R.R., and Feld, M.S. (1997). Single molecule detection using surface-enhanced Raman scattering (SERS). Phys. Rev. Lett. *78*, 1667–1670.

Kneipp, J., Kneippa, H., and Kneippac, K. (2008). SERS—a single-molecule and nanoscale tool for bioanalytics. Chem. Soc. Rev. *37*, 1052–1060.

Li, J.F., Huang, Y.F., Ding, Y., Yang, Z.L., Li, S.B., Zhou, X.S., Fan, F.R., Zhang, W., Zhou, Z.Y., Wu, D.Y., et al. (2010). Shell-isolated nanoparticle-enhanced Raman spectroscopy. Nature *464*, 392–395.

Li, W., Zamani, R., Gil, P.R., Pelaz, B., Ibanez, M., Cadavid, D., Shavel, A., Alvarez-Puebla, R.A., Parak, J.W., Arbiol, J., et al. (2013). CuTe nanocrystals: shape and size control, plasmonic properties, and use as SERS probes and photothermal agents. J. Am. Chem. Soc. *135*, 7098–7101.

Li, J.M., Li, J.Y., Yang, Y., and Qin, D. (2015). Bifunctional Ag@Pd-Ag nanocubes for highly sensitive monitoring of catalytic reactions by surface-enhanced Raman spectroscopy. J. Am. Chem. Soc. *137*, 7039–7042.

Li, T., Chen, K., Chen, Z.F., Cong, C.X., Qiu, C.Y., Chen, J.J., Wang, X.M., Chen, H.J., Yu, T., Xie, W.J., et al. (2018a). 1T′ transition metal telluride atomic Layers for plasmon-free SERS at femtomolar levels. J. Am. Chem. Soc. *140*, 8696–8704.

Li, A.R., Lin, J., Huang, Z.N., Wang, X.T., and Guo, L. (2018b). Surface-enhanced Raman spectroscopy on amorphous semiconducting rhodium sulfide microbowl substrates. iScience *10*, 1–10.

Li, Z.L., Ganapathy, S., Xu, Y.L., Zhou, Z., Sarilar, M., and Wagemaker, M. (2019). Mechanistic insight into the electrochemical performance of Zn/VO_2 batteries with an aqueous $ZnSO_4$ electrolyte. Adv. Energy Mater. *9*, 1900237.

Lin, X.M., Cui, Y., Xu, Y.H., Ren, B., and Tian, Z.Q. (2009). Surface-enhanced Raman spectroscopy: substrate-related issues. Anal. Bioanal. Chem. *394*, 1729–1745.

Lin, J., Shang, Y., Li, X.X., Yu, J., Wang, X.T., and Guo, L. (2017). Ultrasensitive SERS detection by defect engineering on single Cu_2O superstructure particle. Adv. Mater. *29*, 1604797.

Lin, J., Hao, W., Shang, Y., Wang, X.T., Qiu, D.L., Ma, G.S., Chen, C., Li, S.Z., and Guo, L. (2018). Direct experimental observation of facet-dependent SERS of Cu_2O polyhedra. Small *14*, 1703274.

Lombardi, J.R., Birke, R.L., Lu, T.H., and Xu, J. (1986). Charge-transfer theory of surface enhanced Raman spectroscopy: Herzberg–Teller contributions. J. Chem. Phys. *84*, 4174–4180.

Manthiram, K., and Alivisatos, A.P. (2012). Tunable localized surface plasmon resonances in tungsten oxide nanocrystals. J. Am. Chem. Soc. *134*, 3995–3998.

Morrison, V.R., Chatelain, R.P., Tiwari, K.L., Hendaoui, A., Bruhacs, A., Chaker, M., and Siwick, B.G. (2014). A photoinduced metal-like phase of monoclinic VO_2 revealed by ultrafast electron diffraction. Science *346*, 445–448.

Moskovits, M. (1978). Surface roughness and the enhanced intensity of Raman scattering by molecules adsorbed on metals. J. Chem. Phys. *69*, 4159–4161.

Muehlethaler, C., Considine, C.R., Menon, V., Lin, W.C., Lee, Y.H., and Lombardi, G.Y. (2016). Ultrahigh Raman enhancement on monolayer MoS_2. ACS Photon. *3*, 1164–1169.

Mulvihill, M., Tao, A., Benjauthrit, K., Arnold, J., and Yang, P.D. (2008). Surface enhanced Raman spectroscopy for trace arsenic detection in contaminated water. Angew. Chem. Int. Ed. *120*, 6556–6560.

Nethravathi, C., Rajamathi, C.R., Rajamathi, M., Gautam, U.K., Wang, X., Golberg, D., and Bando, Y. (2013). N-doped graphene–VO_2 (B) nanosheet-built 3D flower hybrid for lithium ion battery. ACS Appl. Mater. Interfaces *5*, 2708–2714.

Nie, S., and Emory, S.R. (1997). Probing single molecules and single nanoparticles by surface-enhanced Raman scattering. Science *275*, 1102–1106.

Palonpon, A.F., Ando, J., Yamakoshi, H., Dodo, K., Sodeoka, M., Kawata, S., and Fujita, K. (2013). Raman and SERS microscopy for molecular imaging of live cells. Nat. Protoc. *8*, 677–692.

Park, W.H., and Kim, Z.H. (2010). Charge transfer enhancement in the SERS of a single molecule. Nano Lett. *10*, 4040–4048.

Peksa, V., Jahn, M., Stolcova, L., Schulz, V., Proska, J., Prochazka, M., Weber, K., Cialla-May, D., and Poppet, J. (2015). Quantitative SERS analysis of azorubine (E 122) in sweet drinks. Anal. Chem. *87*, 2840–2844.

Phan-Quang, G.C., Lee, H.K., Phang, Y.Y., and Ling, X.Y. (2015). Plasmonic colloidosomes as three-dimensional SERS platforms with enhanced surface area for multiphase sub-microliter toxin sensing. Angew. Chem. Int. Ed. *54*, 9691–9695.

Qazilbash, M.M., Brehm, M., Chae, B.G., Ho, P.C., Andreev, G.O., Kim, B.J., Yun, S.J., Balatsky, A.V., Maple, M.B., Keilmann, F., et al. (2007). Mott transition in VO_2 revealed by infrared spectroscopy and nano-imaging. Science *318*, 1750–1753.

Qi, D.Y., Lu, L.G., Wang, L.Z., and Zhang, J.L. (2014). Improved SERS sensitivity on plasmon-free TiO_2 photonic microarray by enhancing light-matter coupling. J. Am. Chem. Soc. *136*, 9886–9889.

Qian, X.M., Peng, X.H., Ansari1, D.O., Yin-Goen, Q., Chen, G.Z., Shin, D.M., Yang, L., Young, A.N., Wang, M.D., and Nie, S. (2008). In vivo tumor targeting and spectroscopic detection with surface-enhanced Raman nanoparticle tags. Nat. Biotechnol. *26*, 83–90.

Qiu, B.C., Xing, M.Y., Yi, Q.Y., and Zhang, J.L. (2015). Chiral carbonaceous nanotubes modified with titania nanocrystals: plasmon-free and recyclable SERS sensitivity. Angew. Chem. Int. Ed. *54*, 10643–10647.

Quagliano, L.G. (2004). Observation of molecules adsorbed on III-V semiconductor quantum dots by surface-enhanced Raman scattering. J. Am. Chem. Soc. *126*, 7393–7398.

Schlucker, S. (2014). Surface-enhanced Raman spectroscopy: concepts and chemical applications. Angew. Chem. Int. Ed. *53*, 4756–4795.

Strelcov, E., Lilach, Y., and Kolmakov, A. (2009). Gas sensor based on metal–insulator transition in VO_2 nanowire thermistor. Nano Lett. *9*, 2322–2326.

Sun, H.Z., Cong, S., Zheng, Z.H., Wang, Z., Chen, Z.G., and Zhao, Z.G. (2019). Metal–organic frameworks as surface enhanced Raman scattering substrates with high tailorability. J. Am. Chem. Soc. *141*, 870–878.

Taylor, R.W., Coulston, R.J., Biedermann, F., Mahajan, S., Baumberg, J.J., and Scherman, O.A. (2013). In situ SERS monitoring of photochemistry within a nanojunction reactor. Nano Lett. *13*, 5985–5990.

Wang, X.T., Shi, W.S., She, G.W., and Ma, L.X. (2011). Using Si and Ge nanostructures as substrates for surface-enhanced Raman scattering based on photoinduced charge transfer mechanism. J. Am. Chem. Soc. *133*, 16518–16523.

Wang, X.J., Wang, C., Cheng, L., Lee, S.T., and Liu, Z. (2012). Noble metal coated single-walled carbon nanotubes for applications in surface enhanced Raman scattering imaging and photothermal therapy. J. Am. Chem. Soc. *134*, 7414–7422.

Wang, X.T., Shi, W.X., Jin, Z., Huang, W.F., Lin, J., Ma, G.S., Li, S.Z., and Guo, L. (2017). Remarkable SERS activity observed from amorphous ZnO nanocages. Angew. Chem. Int. Ed. *56*, 9851–9855.

Wang, X.T., Shi, W.X., Wang, S.X., Zhao, H.W., Lin, J., Yang, Z., Chen, M., and Guoet, L. (2019). Two-dimensional amorphous TiO_2 nanosheets enabling high-efficiency photoinduced charge transfer for excellent SERS activity. J. Am. Chem. Soc. *141*, 5856–5862.

Whittaker, L., Jaye, C., Fu, Z., Fischer, D.A., and Banerjee, S. (2009). Depressed phase transition in solution-grown VO_2 nanostructures. J. Am. Chem. Soc. *131*, 8884–8894.

Willets, K.A. (2014). Super-resolution imaging of SERS hot spots. Chem. Soc. Rev. *43*, 3854–3864.

Xi, G.C., Ouyang, S.X., Li, P., Ye, J.H., Ma, Q., Su, N., Bai, H., and Wang, C. (2012a). Ultrathin $W_{18}O_{49}$ nanowires with diameters below 1 nm: synthesis, near-infrared absorption, photoluminescence, and photochemical reduction of carbon dioxide. Angew. Chem. Int. Ed. *51*, 2395–2399.

Xi, G.C., Ye, J.H., Ma, Q., Su, N., Bai, H., and Wang, C. (2012b). In situ growth of metal particles

on 3D urchin-like WO_3 nanostructures. J. Am. Chem. Soc. *134*, 6508–6511.

Xie, L.M., Ling, X., Fang, Y., Zhang, J., and Liu, Z.F. (2009). Graphene as a substrate to suppress fluorescence in resonance Raman spectroscopy. J. Am. Chem. Soc. *131*, 9890–9891.

Yilmaz, M., Babur, E., Ozdemir, M., Gieseking, R.L., Dede, Y., Tamer, U., Schatz, G.C., Facchetti, A., Usta, H., and Demirel, G. (2017). Nanostructured organic semiconductor films for molecular detection with surface-enhanced Raman spectroscopy. Nat. Mater. *16*, 918–924.

Zhang, Y., Qian, J., Wang, D., Wang, Y.L., and He, S.L. (2013). Multifunctional gold nanorods with ultrahigh stability and tunability for in vivo fluorescence imaging, SERS detection, and photodynamic therapy. Angew. Chem. Int. Ed. *52*, 1148–1151.

Zhang, X.Y., Zheng, Y.H., Liu, X., Lu, W., Dai, J.Y., Lei, D.Y., and MacFarlane, D.R. (2015). Hierarchical porous plasmonic metamaterials for reproducible ultrasensitive surface-enhanced Raman spectroscopy. Adv. Mater. *27*, 1090–1096.

Zhang, Q.Q., Li, X.S., Ma, Q., Zhang, Q., Bai, H., Yi, W.C., Liu, J.Y., Han, J., and Xi, G.C. (2017). A metallic molybdenum dioxide with high stability for surface enhanced Raman spectroscopy. Nat. Commun. *8*, 14903.

Zheng, Z.H., Cong, S., Gong, W.B., Xuan, J.N., Li, G.H., Lu, W.B., Geng, F.X., and Zhao, Z.G. (2017). Semiconductor SERS enhancement enabled by oxygen incorporation. Nat. Commun. *8*, 1993.

Zhu, C.H., Meng, G.W., Zheng, P., Huang, Q., Li, Z.B., Hu, X.Y., Wang, X.J., Huang, Z.L., Li, F.D., and Wu, N.Q. (2016). A hierarchically ordered array of silver-nanorod bundles for surface-enhanced Raman scattering detection of phenolic pollutants. Adv. Mater. *28*, 4871–4876.

ISCI, Volume *19*

Supplemental Information

Quasi-Metal for Highly Sensitive and Stable Surface-Enhanced Raman Scattering

Zheng Tian, Hua Bai, Chao Chen, Yuting Ye, Qinghong Kong, Yahui Li, Wenhao Fan, Wencai Yi, and Guangcheng Xi

Supplemental Information

1. Transparent Methods

Synthesis of b-VO_2 nanosheets

All chemicals used in the experiments are of analytical purity. In a typical synthesis, 0.1 g of vanadyl acetylacetonate (VAA) is dissolved in 30 mL of absolute ethanol to form a bright blue transparent solution. The resulting homogeneous solution is then transferred to a Teflon-lined high-pressure reactor, and a common glass sheet is placed above the liquid level as a growth platform for b-VO_2 nanosheets. The Teflon-lined stainless steel autoclave was sealed and heated for 20 h at 200 °C. After the reaction is completed, the glass sheet covered with black products was taken out. Finally, the black glass was washed with ethanol and distilled water for three times and dried at 50 °C in a vacuum drying oven.

Synthesis of SiO_2/VO_2

Open a bottle of analytically pure silicon tetrachloride ($SiCl_4$) in air. Soon, a lot of "white-fog" formed at the mouth of the bottle. Place the glass sheet covered with VO_2 nanosheets in a white mist at the mouth of the bottle for 3 min. Then, the glass sheet is placed in a nitrogen-protected tubular furnace and heated to 400 °C for 1 hours. After natural cooling, take out for use.

Synthesis of urchin-like $W_{18}O_{49}$ nanostructures

In a typical procedure, 3 g of WCl_6 was dissolved in 100 mL of ethanol, and the obtained yellow solution was magnetically stirred for 20 min, and then transferred to a Teflon-lined stainless-steel autoclave and heated at 200 °C for 20 h with a heating rate

of 4 °C/min. The autoclave was cool down naturally and a blue product was collected, washed, and dried in a vacuum drying oven at 50 °C for 4 h.

Characterization

These samples were measured by a variety of characterization techniques. XRD patterns of the products were obtained on a Bruker D8 focus X-ray diffractometer by using CuKa radiation (λ = 1.54178 Å). SEM images and EDS were obtained on a Hitachi S-4800. TEM and HRTEM characterizations were performed with a Tecnai G F30 operated at 300 kV. Ultraviolet–Vis (UV) absorption spectra were recorded with a Shimadzu UV3600. XPS were recorded on an ESCALab-250Xi of ThermoFisher Scientific. The Fourier transform infrared spectra were measured from THERMO Iz-10. The specific surface area was measured in a Micro Tristar II 3020. The work functions of b-VO_2 nanosheets was detected from Kelvin probe force microscope, Multimode-Picoforce-Veeco. ESR spectrum was obtained from ESP-300.

Raman tests

To study the SERS of these b-VO_2 nanosheets, a confocal micro Raman spectrometer (Renishaw-inVia Reflex) is used as the measuring instrument. In all SERS tests, unless specifically stated, the excitation wavelength is 532 nm, laser power is 0.5 mW and the specification of the objective is × 50 L. A series of standard solution (aqueous) of highly risk chemical with concentrations of 10^{-7}-10^{-10} M were used as the probe molecules. To improve the signal reproducibility and uniformity, before each test, the glass sheet (1 cm × 1 cm) covered with b-VO_2 nanosheets were immersed into a 20 mL of probe solution with specific concentration for 20 min, then taken out and dried

in air for 20 min. In all SERS tests, the laser beam is perpendicular to the top of the sample to be tested with a resultant beam spot diameter of 5 μm. The calculation of EF are provided in Supplementary Methods.

Enhanced Factor Calculation

To calculate the EF of the b-VO_2 nanosheets, the ratio of SERS to normal Raman spectra (NRS) of RH6G was determined by using the following calculating formula 1

$$EF = (I_{SERS}/I_{NRS}) \times (C_{NRS}/C_{SERS}) \quad (1)$$

where I_{SERS} and I_{NRS} refer to the peak intensities of the SERS and NRS, respectively. C_{NRS} and C_{SERS} refer to the concentrations of the probe molecules of the NRS and SERS, respectively. In the SERS measurements, two Raman scattering peaks, R_1 at 612 cm^{-1} and R_2 at 773 cm^{-1} were selected for the calculations of the EF. For comparison, the peak intensities of the R6G (1×10^{-2} M, aqueous solution) directly placed on bare glass slide were detected as NRS data. For the NRS data, the integration time is 4000 s, while for the SERS data, the integration time is 10 s.

Calculations details

All the density functional theory (DFT) calculations were carried out using the Vienna Ab initio Simulation Package (VASP)[1-3]. The Perdew-Burke-Ernzerhof (PBE) was used to describe the exchange-correlation[4]. The optimization process was performed using a conjugate gradient algorithm with a force tolerance of 0.02 eV/Å, with kinetic energy cutoff set as 500 eV. A Gamma k-point sampling of 3 × 7 × 5 was used to optimize the VO_2 cell parameters. The optimized lattice parameters were 11.99, 3.74, 6.40 Å, and 90.0, 107.0, 90.0°, respectively.

To calculate the VO_2 (112) surface, a $2 \times 2 \times 1$ supercell was built by cut the original cell along (112) facet, with a 20 Å additional vacuum layer in z-direction. Thus, the lattice parameter of the layer slab model was 24.82 Å × 19.68 Å × 26.97 Å. A 2D-shaped graphene layer was calculated to adsorb RH6G molecule as well, containing 200 carbon atoms, with the supercell parameters equal to 24.47 Å × 24.67 Å × 20 Å and 90, 90, 120°, respectively. The structure of RH6G molecule was optimized in the same cell as well. For these simulations, the plane wave cutoff energy set as 500 eV and the k-point mesh set as 1 × 1 × 1.

1. Kresse, G., and Hafner, J. (1994). Ab initio molecular-dynamics simulation of the liquid-metal–amorphous-semiconductor transition in germanium. Phys. Rev. B *49*, 14251-14269 .

2. Kresse, G., and Furthmüller, J. (1996). Efficiency of ab-initio total energy calculations for metals and semiconductors using a plane-wave basis set. J. Comp. Mater. Sci. *6*, 15-50.

3. Kresse, G., and Furthmüller, (1996). J. Efficient iterative schemes for ab initio total-energy calculations using a plane-wave basis set. Phys. Rev. B *54*, 11169-11186.

4. Perdew, J. P., Burke, K., and Ernzerhof, M. (1996). Generalized gradient approximation made simple. Phys. Rev. Lett. *77*, 3865-3868 .

2. Supporting Figures

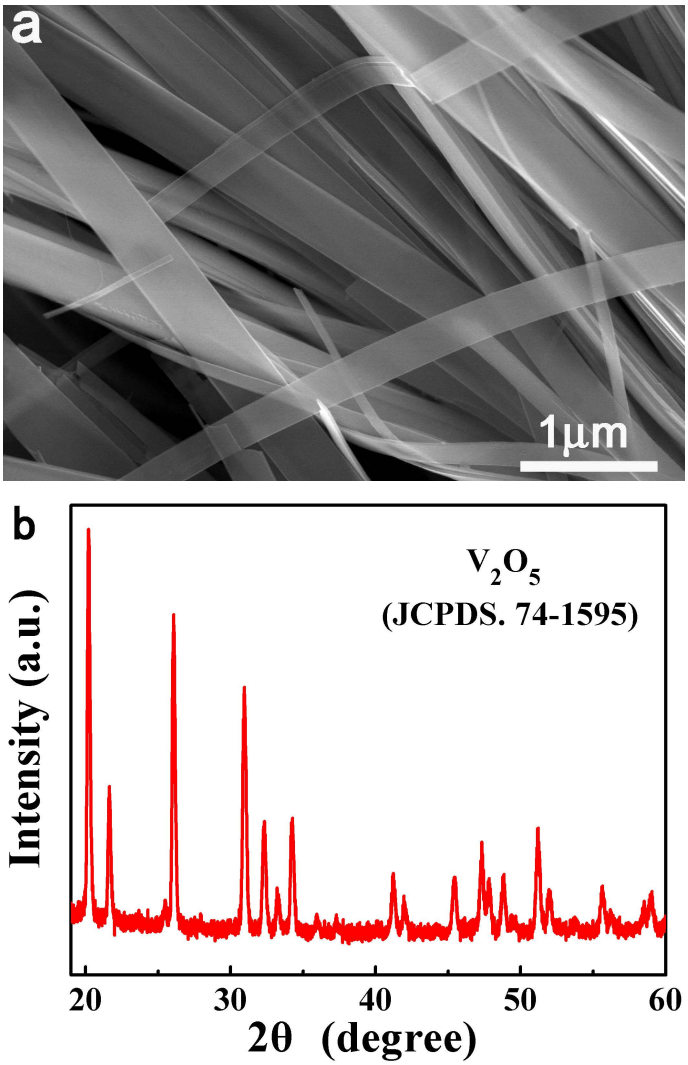

Figure S1. SEM image (a) and XRD pattern (b) of the V_2O_5 nanobelts obtained when ethanol is replaced by deionized water. Related to Figure 1.

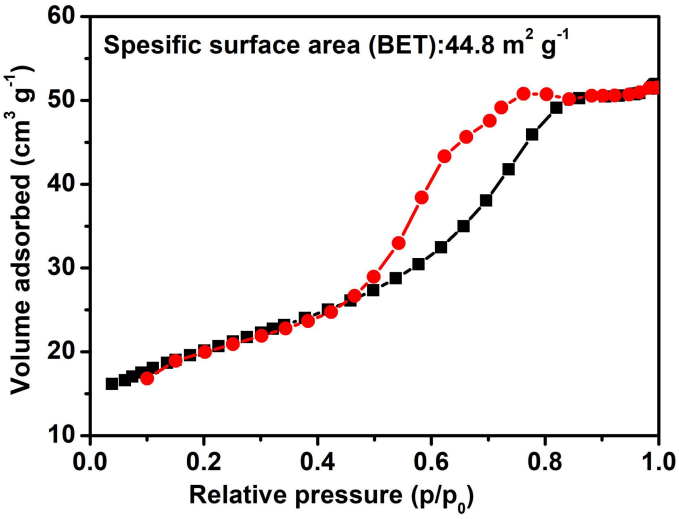

Figure S2. N_2 adsorption/desorption isotherms of the as-synthesized b-VO_2 nanosheets, related to Figure 1.

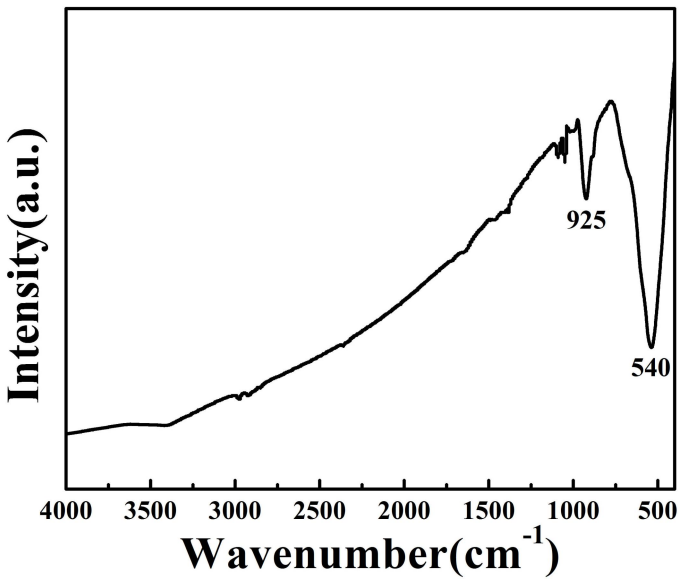

Figure S3. FTIR spectrum of the as-synthesized b-VO_2 nanosheets, related to Figure 1.

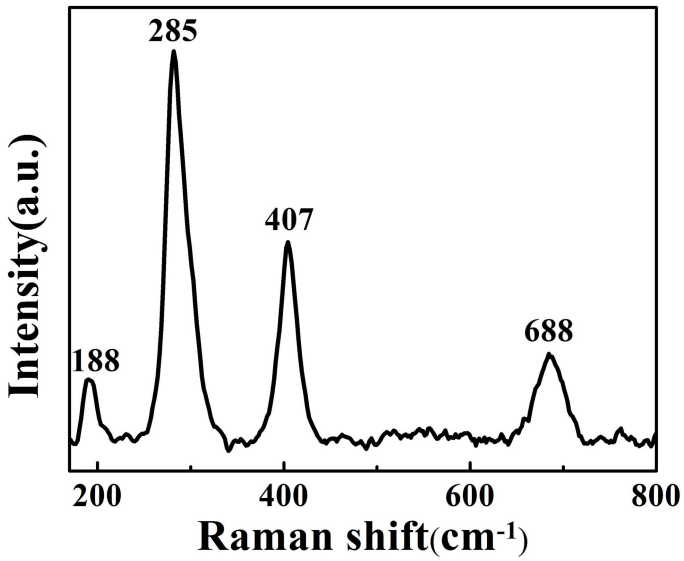

Figure S4. Raman spectrum of the b-VO_2 nanosheets, related to Figure 1.

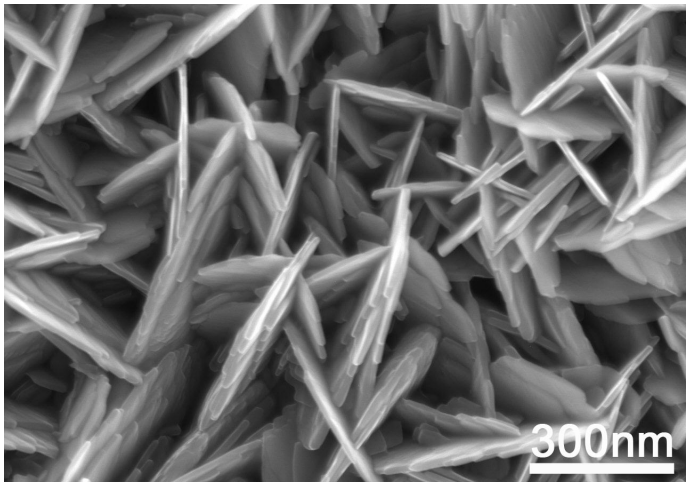

Figure S5. TEM image of the V_2O_5 nanosheets prepared by heating the b-VO_2 nanosheets at 400 °C, related to Figure 2.

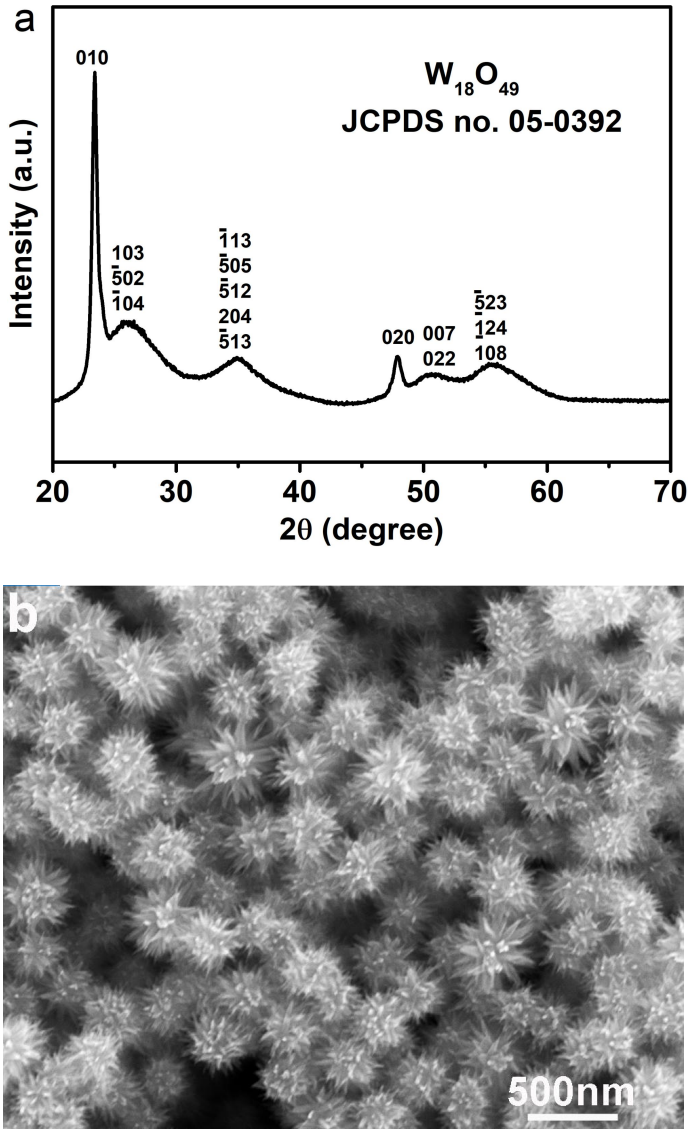

Figure S6. XRD pattern (a) and SEM image (b) of the prepared urchin-like $W_{18}O_{49}$ nanostructures. Related to Figure 2.

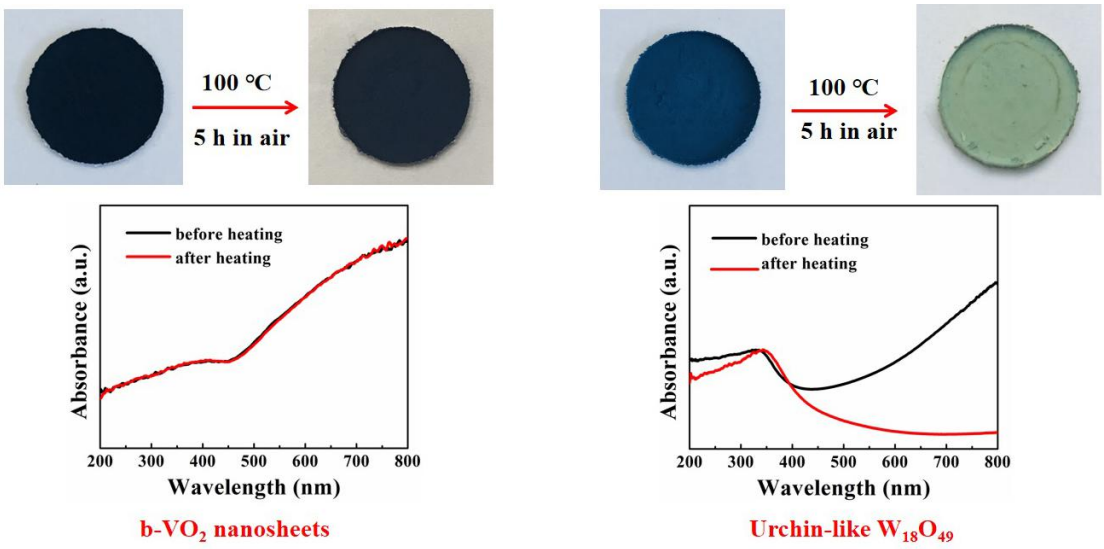

Figure S7. The comparison of oxidation resistance between b-VO_2 and $W_{18}O_{49}$. The change of color and absorbance before and after heating from two kinds of samples clearly indicated that the oxidation resistance of $W_{18}O_{49}$ is much lower than that of b-VO_2. Related to Figure 2.

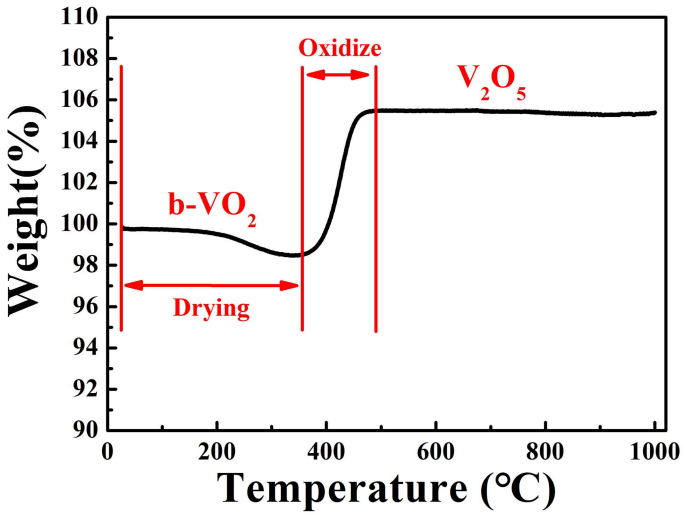

Figure S8. The differential thermal analysis (DTA) curve of the b-VO_2 nanosheets. Below 350 °C, the b-VO_2 nanosheets are stable. When the temperature continues to rise, they were gradually oxidized to V_2O_5. Related to Figure 2.

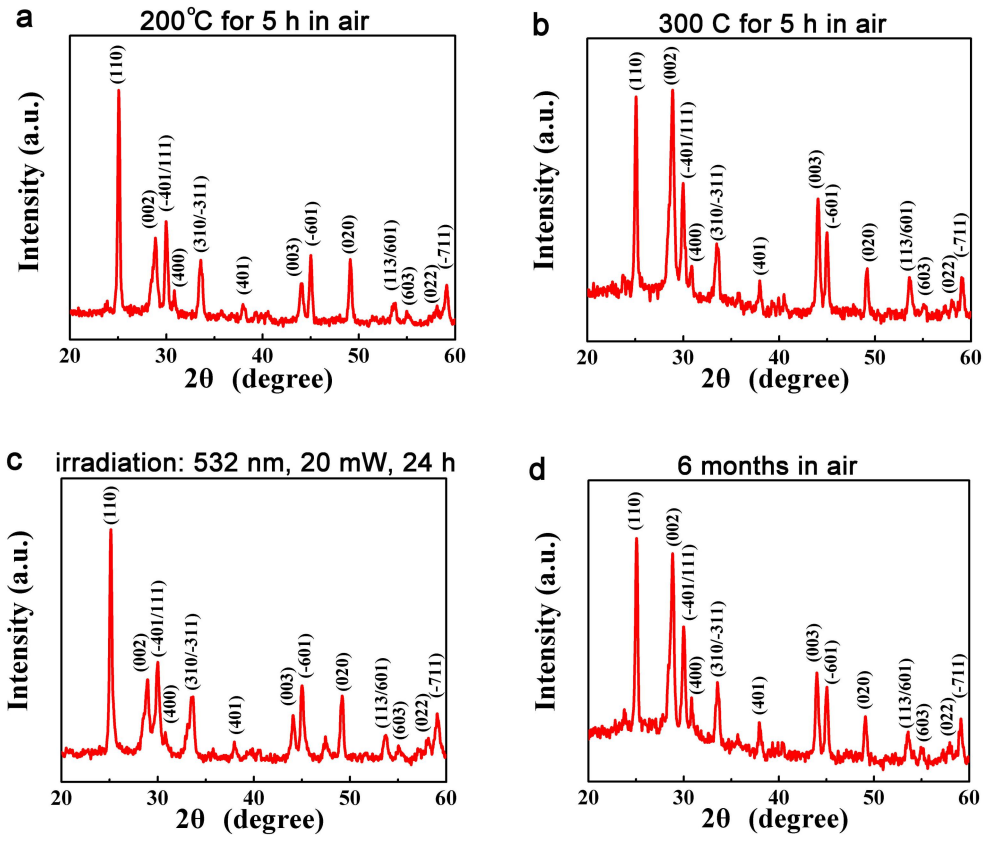

Figure S9. A series of XRD patterns demonstrated that no detectable change in the XRD patterns of b-VO_2 nanosheets after the heating, irradiating, and long-term storage. Related to Figure 2.

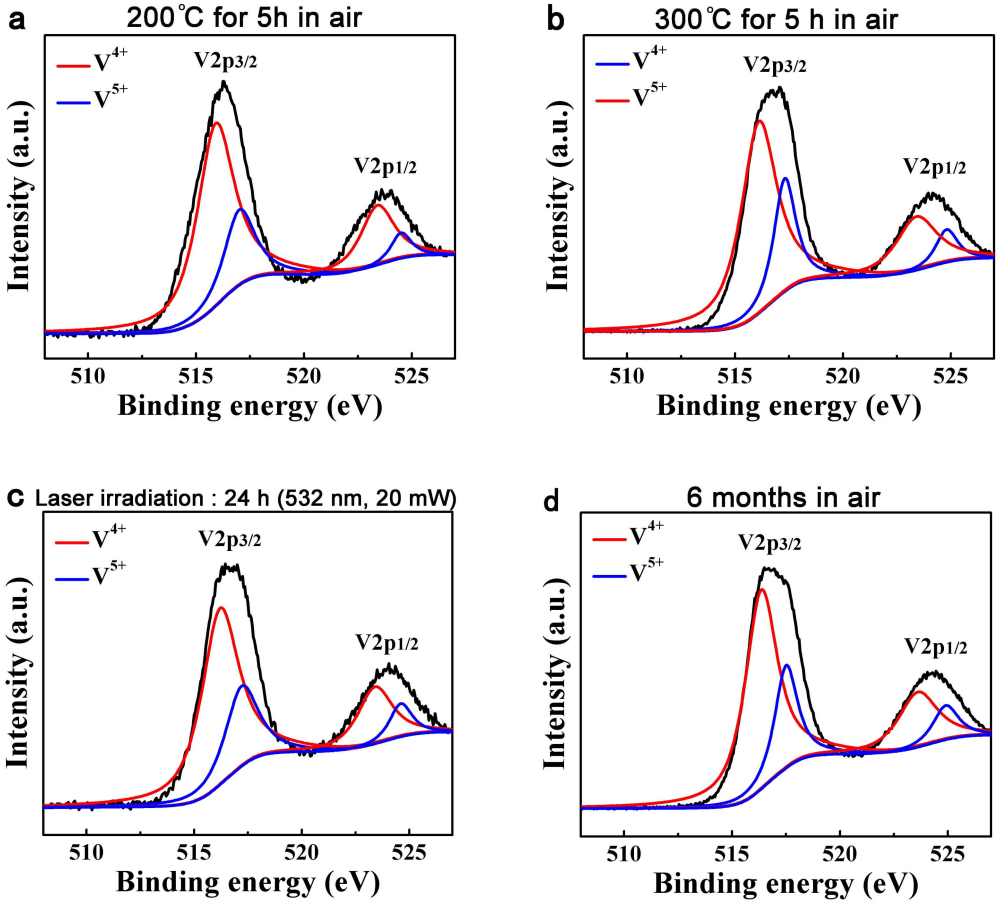

Figure S10. A series of XPS spectra demonstrated that no detectable change in the valence state of the b-VO_2 nanosheets after the heating, irradiation, and long-term storage. The XPS and XRD (Figure S6) results demonstrate that the stability of these b-VO_2 nanosheets is extraordinary high. Related to Figure 2.

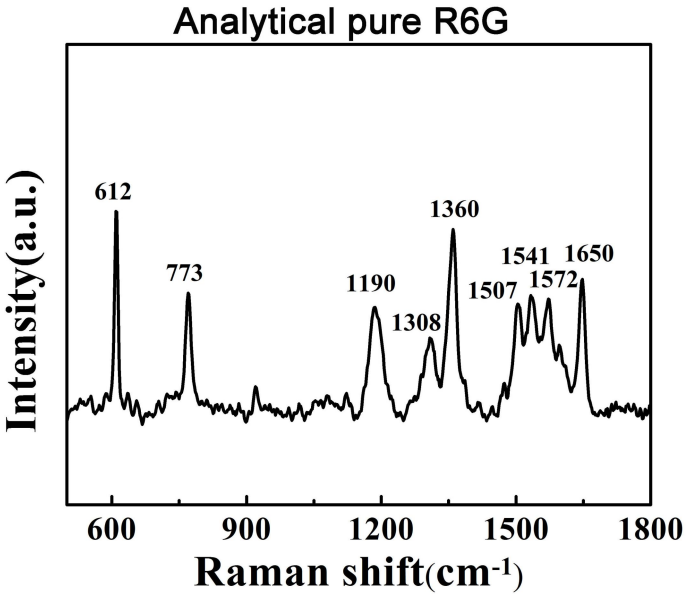

Figure S11. The standard Raman spectrum of R6G reference material, related to Figure 3.

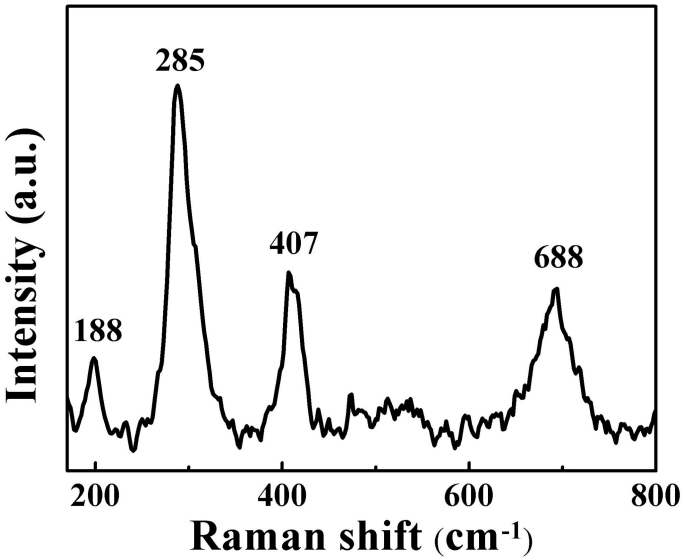

Figure S12. The bare b-VO_2 nanosheet arrays without R6G solution only showed the typical Raman scattering peaks of themself, related to Figure 3.

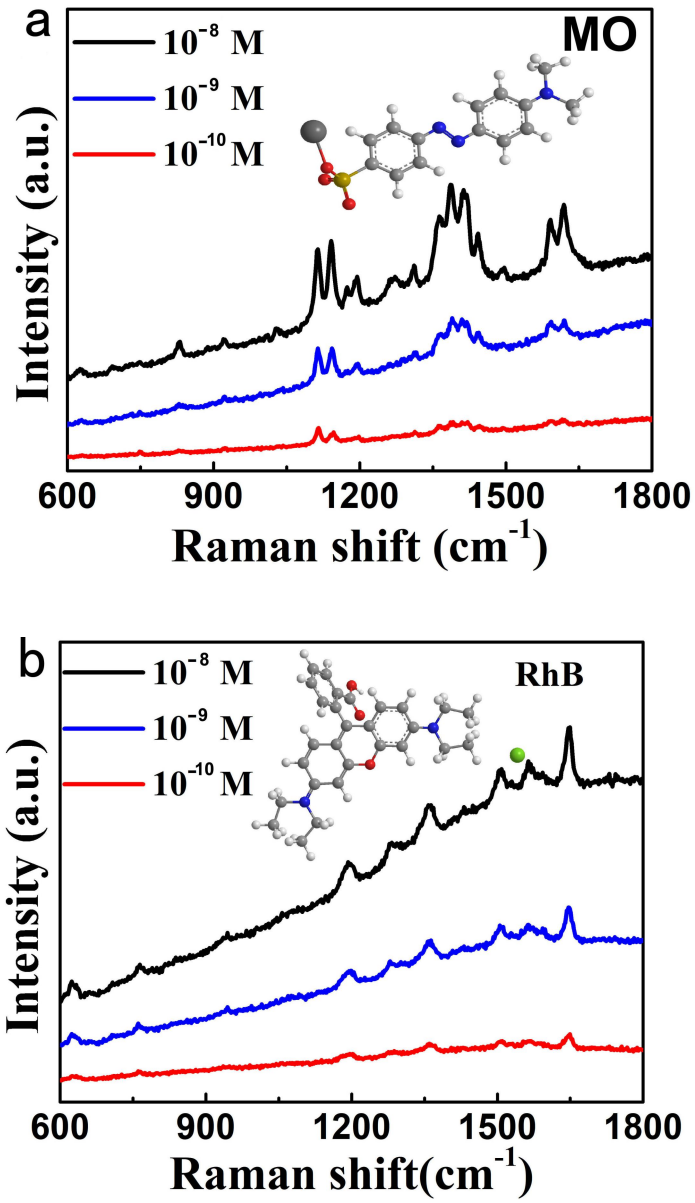

Figure 13. SERS spectra of the dye molecules of MO (a) and RhB (b). Related to Figure 3.

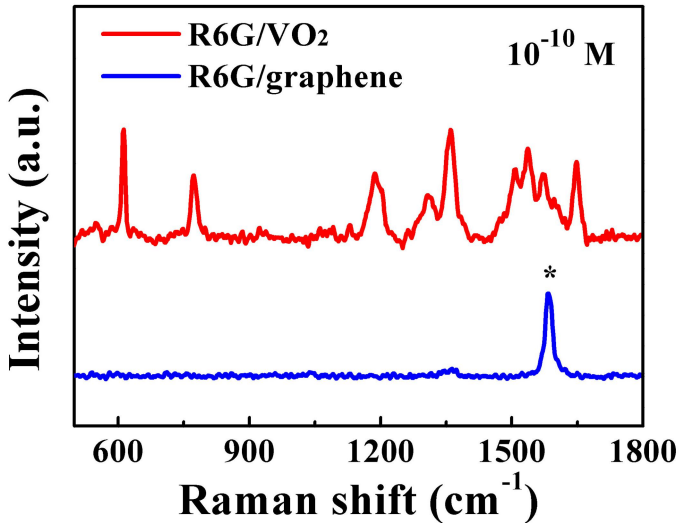

Figure S14. SERS spectra of 10^{-10} M R6G on b-VO_2 nanosheets and graphene, respectively, related to Figure 6.

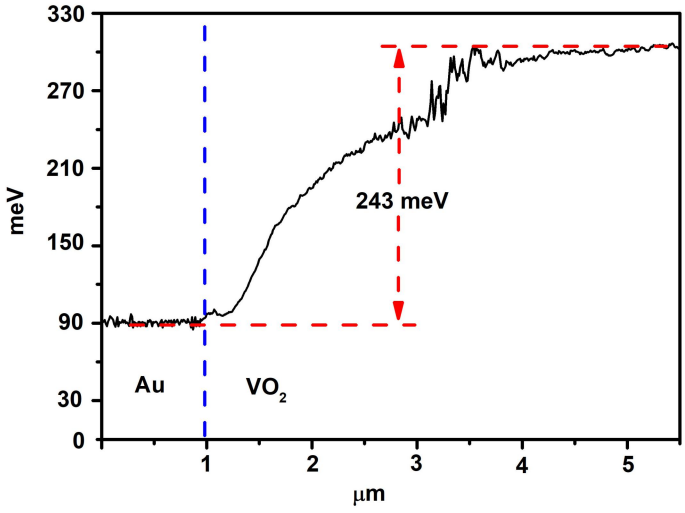

Figure S15. The measured surface potential difference profiles. Considering that the work function of Au reference is 4.8 eV, the work function of b-VO_2 nanosheets is estimated to be 4.55 eV. The b-VO_2 thickness dependence on its work function can be neglected. Related to Figure 6.

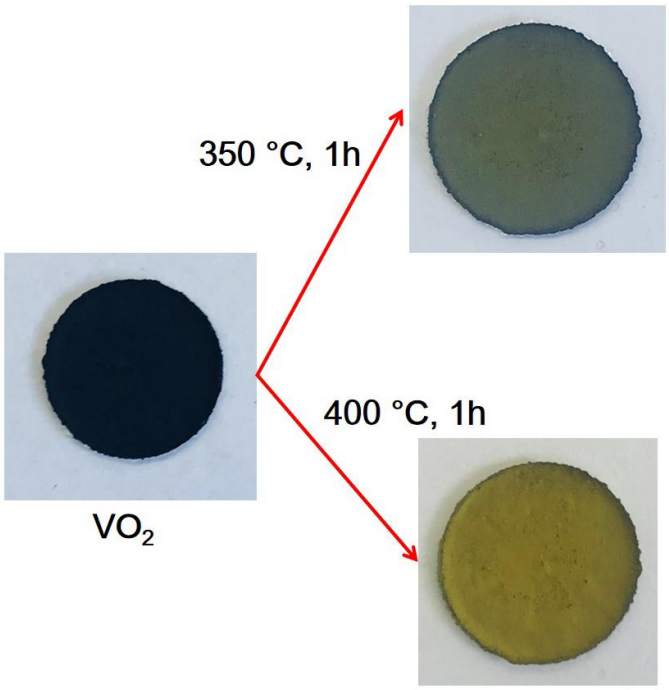

Figure S16. When these b-VO_2 nanosheets were heated in air for a period of time, their colors have changed dramatically. Related to Figure 6.

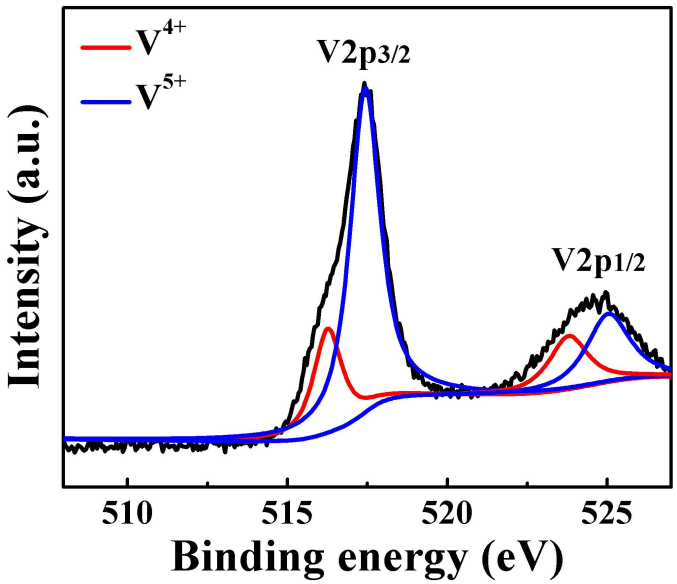

Figure S17. The XPS spectrum of the sample after heating at 400 °C for 1h in air, which suggests that the VO_2 has been transformed into V_2O_5. Related to Figure 6.

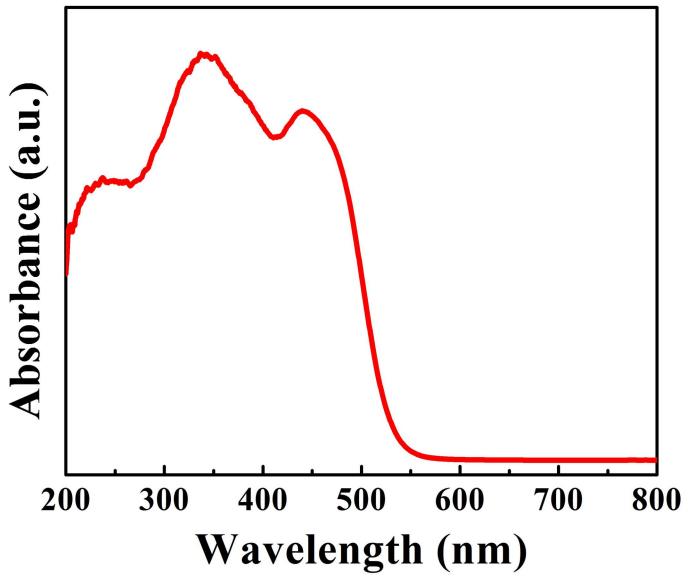

Figure S18. The UV-Vis absorption of the sample after heating at 400 °C for 1h in air, related to Figure 6.

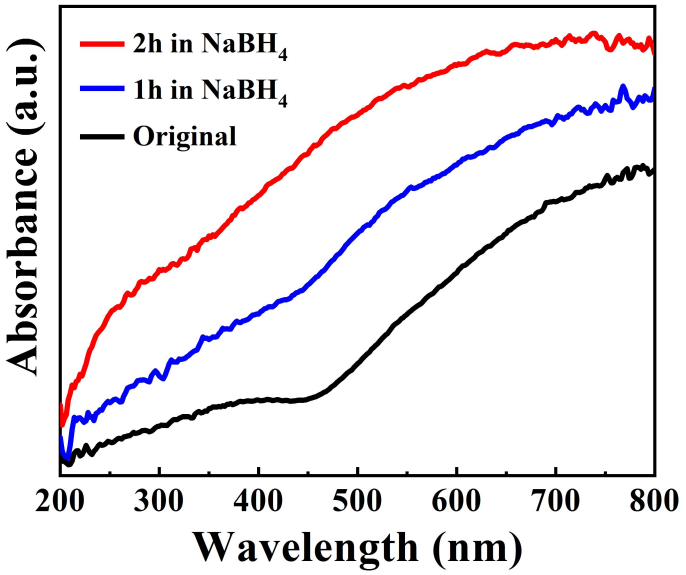

Figure 19. The UV-Vis absorption of the VO_2 samples reduced by $NaBH_4$ aqueous solution, related to Figure 6.

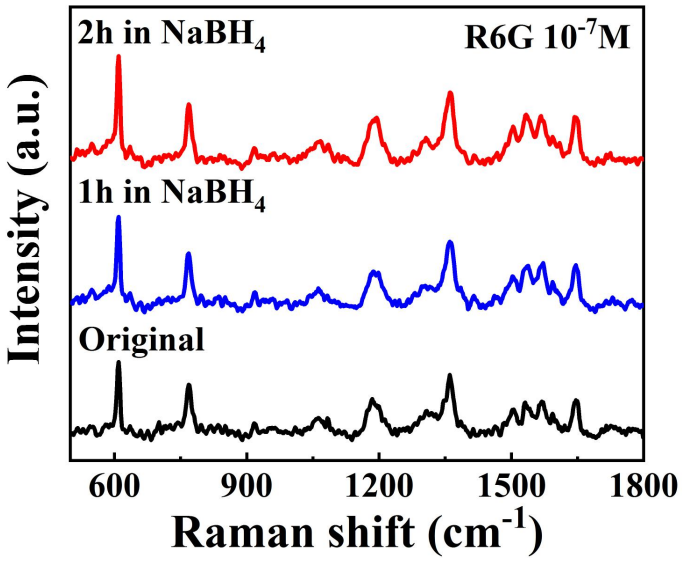

Figure S20. The obtained SERS signals from the reduced VO_2 nanosheet substrates, related to Figure 6.

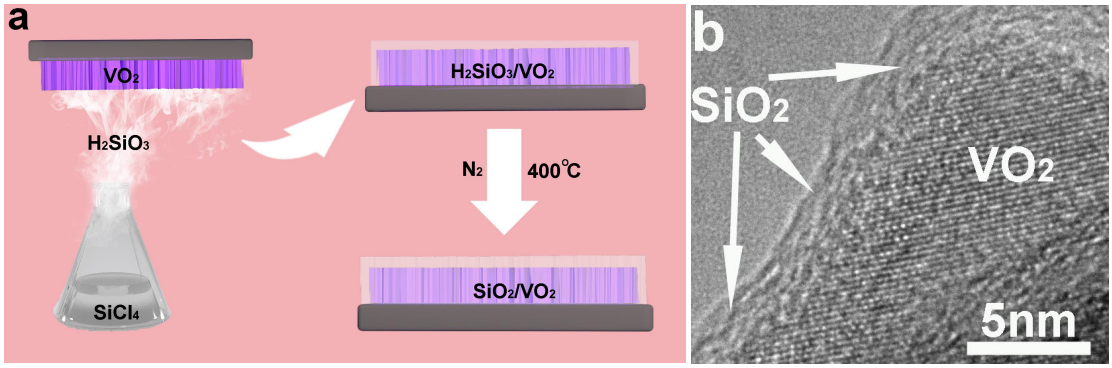

Figure 21. (a) Schematic illustrating the synthesis of the SiO_2/VO_2. $SiCl_4$ is easily hydrolyzed into H_2SiO_3 in air. These formed H_2SiO_3 species were coated on VO_2 nanosheets and formed H_2SiO_3/VO_2. The VO_2 nanosheets coated with amorphous SiO_2 layers were obtained by heating under N_2 protection. (b) The HRTEM image of the obtained SiO_2/VO_2, revealing the thickness of SiO_2 layer is about 2 nm. Related to Figure 6.

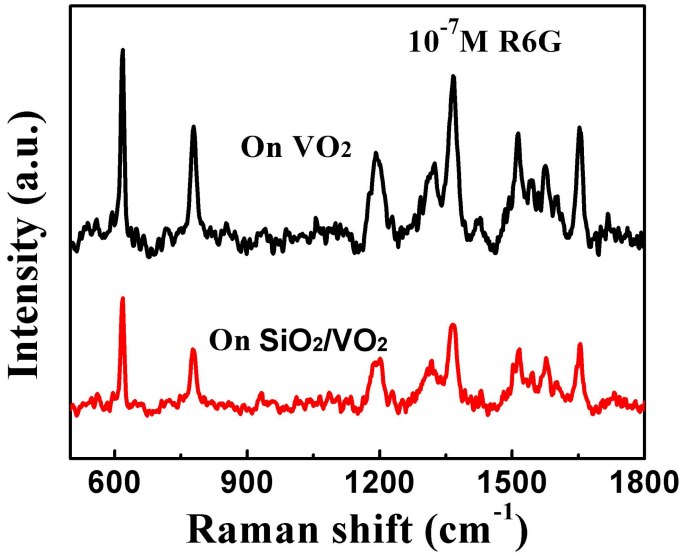

Figure S22. (a) The obtained SERS signals from VO_2 nanosheet substrate and SiO_2/VO_2 substrate, respectively. Related to Figure 6.

Table S1: Some of the previously reported EFs for Non-Noble Metal Enhanced Raman Substrate materials, related to Figure 3

Substrate	Probe molecule	Excited wavelength (nm)	Author	EF	Detectable Limit (M)	Stability
TiO_2	MB	532	D. Qi et al., 2014	2×10^4	10^{-5}	stable
CdTe	4-Mpy	514.5	Y. F. Wang et al., 2007	10^4	10^{-3}	Liable to oxidation and corrosion
ZnO	D266	488	H. Wen et al., 1996	50	10^{-5}	Liable to corrosion
CdS	4-Mpy	514.5	Y. F. Wang et al., 2008	10^2	10^{-3}	Liable to oxidation and corrosion
α -Fe_2O_3	4-Mpy	514.5	X. Q. Fu et al., 2009	2.7×10^4	10^{-3}	Liable to corrosion
Cu_2O	4-MBA	488	L. Jiang et al., 2013	10^5	10^{-3}	Liable to oxidation and corrosion
CuO	4-Mpy	514.5	Y. Wang et al., 2007	10^2	10^{-1}	Liable to corrosion
$W_{18}O_{49}$	R6G	532.8	S. Cong et al., 2015	3.4×10^5	10^{-7}	Liable to oxidation
Cu_2O	R6G	532	L. Guo et al., 2017	8×10^5	10^{-9}	Liable to oxidation and corrosion
ZnO	4-MBA	633	Wang, X. T. et al., 2017	6.6×10^5		Liable to corrosion
MoS_2	R6G	532.8	Zheng, Z. H. et al., 2017	1.6×10^5	10^{-7}	Liable to oxidation
						Liable to

MOF	R6G	532.8	Sun, H. Z. et al., 2019	10^6	10^{-8}	oxidation and corrosion
Organic Semiconductor	DFH-4T	532	Yilmaz M. et al., 2017	3.4×10^3	10^{-5}	Liable to oxidation and corrosion
Nb_2O_5	MB	532	Shan, Y. F. et al., 2017	7.1×10^6	10^{-9}	stable
WTe_2/WTe_2	R6G	532	Tao, L. et al., 2018	6.2×10^9	10^{-15}	Liable to oxidation and corrosion
MoO_2	R6G	532	Zhang, Q. et al., 2017	3.75×10^6	10^{-7}	stable
b-VO_2	**R6G**	**532**	**Tian, Z. et al (this work)**	**6.7×10^7**	**10^{-10}**	stable

Qi, D., Lu, L., Wang, L., and Zhang, J. (2014). Improved SERS sensitivity on plasmon-free TiO_2 photonic microarray by enhancing light-matter coupling. J. Am. Chem. Soc. *136*, 9886–9889.

Wang, Y. F., Suna, Z. H., Wanga, Y. X., Hua, H. L., Zhaoa, B., Xua, W. Q., and Lombardi, G. R. (2007). Surface-enhanced Raman scattering on mercaptopyridine-capped CdS microclusters. Spectrochim. Acta, Part A. *66*, 1199–1203.

Wen, H., He, T. J., Xu, C. Y., Zuo, J., and Liu, F. C. (1996). Surface enhancement of Raman and absorption spectra from cyanine dye D266 adsorbed on ZnO colloids. Molecular Physics. *88*, 281–290.

Wang, Y. F., Zhang, J. H., Jia, H. Y., Li, M. J., Zeng, J. B., Yang, B., Zhao, B., and Xu, W. Q. (2008). Mercaptopyridine surface-functionalized CdTe quantum dots with

enhanced Raman scattering properties. J. Phys. Chem. C. *112*, 996–1000.

Fu, X. Q., Bei, F. L., Wang, X., Yang, X. J., and Lu, L. D. (2009). Surface-enhanced Raman scattering of 4-mercaptopyridine on sub-monolayers of α-Fe_2O_3 nanocrystals (sphere, spindle, cube). J. Raman Spectrosc. *40*, 1290–1295.

Jiang, L.,You, T. T., Yin, P. J., Shang, Y., Zhang, D. F., Guo, L., and Yang, S. (2013). Surface-enhanced Raman scattering spectra of adsorbates on Cu_2O nanospheres: charge-transfer and electromagnetic enhancement. Nanoscale. *5*, 2784–2789.

Wang, Y., Hu, H. L., Jing, S. Y., Wang, Y. X., Sun, Z. H., Zhao, B., Zhao, C., and Lombardi, J. R. (2007). Enhanced Raman scattering as a probe for 4-mercaptopyridinesurface-modified copper oxide nanocrystals. Anal. Sci. *23*, 787–791.

Cong, S., Yuan1, Y. Y., Chen, Z. G., Hou, J. Y., Yang, M., Su, Y. L., Zhang, Y. Y., Li, L., Li, Q. W., Geng, F. X., and Zhao, Z. G. (2015). Noble metal-comparable SERS enhancement from semiconducting metal oxides by making oxygen vacancies. Nat. Commun. *6*, 7800.

Lin, J., Shang, Y., Li, X. X., Yu, J., Wang, X. T., and Guo L. (2017). Ultrasensitive SERS detection by defect engineering on single Cu_2O superstructure particle. Adv. Mater. *29*, 1604797.

Guo, L., Wang, X. T., Shi, W. X., Jin, Z., Huang, W. F., Lin, J., Ma, G. S., and Li, S. Z. (2017). Remarkable SERS activity observed from amorphous ZnO nanocages. Angew. Chem. Int. Ed. *56*, 9851–9855.

Zheng, Z. H., Cong, S., Gong, W. B., Xuan, J. N., Li, G. H., Lu, W. B., Geng F. X.,

and Zhao Z. G. (2017). Semiconductor SERS enhancement enabled by oxygen incorporation. Nat. Commun. *8*, 1993.

Sun, H. Z., Cong, S., Zheng, Z. H., Wang, Z., Chen, Z. G., and Zhao, Z. G. (2019). Metal–organic frameworks as surface enhanced Raman scattering substrates with high tailorability. J. Am. Chem. Soc. *141*, 870–878.

Yilmaz, M., Babur, E., Ozdemir, M., Gieseking, R. L., Dede, Y., Tamer, U., Schatz, G. C., Facchetti, A., Usta, H., and Demirel, G. (2017). Nanostructured organic semiconductor films for molecular detection with surface-enhanced Raman spectroscopy. Nat. Mater. *16*, 918–924.

Shan, Y. F., Zheng, Z. H., Liu, J. J., Yang, Y., Li, Z. Y., Huang, Z. R., and Jiang D. L. (2017). Niobium pentoxide: a promising surface-enhanced Raman scattering active semiconductor substrate. npj Comput. Mater. *3*, 11.

Li, T., Chen, K., Chen, Z. F., Cong, C. X., Qiu, C. Y., Chen, J. J., Wang, X. M., Chen, H. J., Yu, T., Xie, W. J., et al. (2018). 1T' transition metal telluride atomic Layers for plasmon-free SERS at femtomolar levels. J. Am. Chem. Soc. *140*, 8696–8704.

Zhang, Q. Q., Li, X. S., Ma, Q., Zhang, Q., Bai, H., Yi, W. C., Liu, J. Y., Han, J., and Xi, G. C. (2017). A metallic molybdenum dioxide with high stability for surface enhanced Raman spectroscopy. Nat. Commun. *8*, 14903.